Revealing the Predominant Surface Facets of Rough Cu Electrodes Under Electrochemical Conditions

Charuni M. Gunathunge, Jingyi Li, Xiang Li, Julie J. Hong, and Matthias M. Waegele*

Department of Chemistry, Merkert Chemistry Center, Boston College, Chestnut Hill, Massachusetts 02467, United States

* E-mail: waegele@bc.edu

Abstract

Metal electrodes with rough surfaces are often found to convert CO or CO_2 to hydrocarbons and oxygenates with high selectivity and at high reaction rates in comparison with their smooth counterparts. The atomic-level morphology of a rough electrode is likely one key factor responsible for its comparatively high catalytic selectivity and activity. However, few methods are capable of probing the atomic-level structure of rough metal electrodes under electrocatalytic conditions. As a result, the nuances in the atomic-level surface morphology that control the catalytic characteristics of these electrodes remain largely unexplored. Because the C≡O stretch frequency of atop-bound CO (CO_{atop}) depends on the coordination of the underlying metal atom, the IR spectrum of this reaction intermediate on the copper electrode could, in principle, provide structural information about the catalytic surface during electrolysis. However, other effects, such as dynamical dipole coupling, easily obscure the dependence of the frequency on the surface morphology. Further, in the limit of low CO_{atop} coverage, where coupling effects are small, the C≡O stretch frequencies of CO_{atop} on Cu(111) and Cu(100) facets are virtually identical. Therefore, on the basis of the C≡O stretch frequency, it is not straightforward to distinguish between these two ubiquitous surface facets, which exhibit vastly different CO reduction activities. Herein, we show that key features of the atomic-level surface morphology of rough copper electrodes can be inferred from the potential-dependence of the lineshape of the C≡O stretch band of CO_{atop}. Specifically, we compared two types of rough copper thin film electrodes that are routinely employed in the context of surface-enhanced infrared absorption spectroscopy (SEIRAS). We found that copper films that are electrochemically deposited on Si-supported Au films (CuAu-Si) are poor catalysts for the reduction of CO to ethylene in comparison to copper films (Cu-Si) that are electrolessly deposited onto Si crystals. As quantified by differential electrochemical mass spectrometry (DEMS), the onset potential for ethylene is $\approx 200 \pm 65$ mV more cathodic for CuAu-Si than that for Cu-Si. To reveal the origin of the disparate catalytic properties of Cu-Si and CuAu-Si, we probed the surfaces of the electrodes with cyclic voltammetry (CV) and SEIRAS. The CV characterization suggests that the (111) surface facet predominates on CuAu-Si, whereas the (100) facet is more common on Cu-Si. SEIRAS reveals that the lineshape of the C≡O stretch of CO_{atop} is composed of two bands that are attributable to CO_{atop} on terrace and defect sites. The different surface structures manifest themselves in the form of starkly differ-

ent potential-dependencies of the lineshape of the C≡O stretch mode of CO_{atop} on the two types of electrodes. With a simple Boltzmann model that considers the different adsorption energies of CO_{atop} on terrace and defect sites, and the resulting CO_{atop} populations on terrace and defect sites, we deduced that the observed electrode-specific potential-dependence of the lineshape is consistent with the presence of different predominant terrace sites on the two types of films. This strategy for assessing the atomic-level morphology is not restricted to SEIRAS, but could also be applied to the C≡O stretch bands recorded with surface-enhanced Raman spectroscopy (SERS), which is suitable for probing a wide range of rough copper electrodes. Therefore, with this work, we establish the potential-dependence of the C≡O stretch band of CO_{atop} as a probe of the atomic-level surface structure of rough metal electrodes under electrochemical conditions. When coupled with complementary techniques, this methodology provides essential structural information for improving further the reaction selectivity of rough metal electrodes.

KEYWORDS: carbon monoxide reduction, copper thin films, SEIRAS, electrocatalysis, CO stretch lineshape, surface morphology.

Introduction

Metal electrodes of high surface roughness often display high conversion rates for CO and CO_2 to desirable reduction products with good reaction selectivity. The strategies that have been employed for the preparation of high-surface area electrodes include the deposition of nanoparticles,[1–5] reduction of variously prepared metal oxide phases,[6–12] halide-induced surface reconstruction,[13–18] electrodeposition,[19–22] and the use of porous supports.[23,24]

The resulting electrodes are among the most selective and efficient catalysts for the reduction of CO and CO_2. For example, the electrodeposition of copper and copper alloy films in the presence of the nucleation inhibitor 3,5-diamino-1,2,4-triazole results in electrocatalysts with high surface area and tunable surface morphology.[19,21] Copper nanowire electrodes produced by this method reduce CO_2 to ethylene with a Faradaic efficiency (F.E.) of $\approx 40\%$ at a potential of -0.5 V versus the reversible hydrogen electrode (RHE). By comparison, $\approx 1\%$ F.E. for ethylene was observed on a polycrystalline Cu foil at the same potential.[19] Similarly, oxide-derived copper electrodes convert CO to C_{2+}-oxygenates with a F.E. of close to $\approx 60\%$ at moderate overpotentials (-0.25 to -0.5 V versus RHE), whereas only $\approx 10\%$ F.E. for these products was reported on a polycrystalline Cu foil in the same potential range.[6]

The favorable catalytic properties of these electrodes are thought to arise from a combination of factors that include the predominance of certain surface facets,[3,14,25] a suitable surface-density of edge and kink sites,[1,3,14,26,27] the presence of subsurface oxygen or partially oxidized copper species,[18,22,28] and a synergistic interplay between electrode morphology and electrolyte that brings about interfacial conditions favorable for the reduction of CO and CO_2.[20,23,29]

The attribution of the observed catalytic activity for CO and CO_2 reduction to specific atomic-level characteristics of high-surface area electrodes has proven challenging, though. For example, the high selectivity for C_{2+} hydrocarbons and oxygenates of oxide-derived copper electrodes have been variably attributed to the presence of metastable copper sites in the vicinity of grain boundaries,[30] the preferential occurrence of (100) surface facets,[25] or the presence of residual oxygen at or below the surface.[28,31] Other studies suggested the absence of such oxygen species.[32–34] Further, a recent report indicated that high-surface area electrodes primarily bring about a favorable product spectrum through the suppression of the hydrogen evolution reaction rather than the promotion of the reduction of CO.[12]

These diverging views highlight the great challenge that lies in identifying the key characteristics of rough electrodes that engender their high catalytic activity and selectivity. One of the key obstacles is the relative scarcity of methods that are suitable for the characterization of these complex materials under elec-

trocatalytic conditions. While *ex situ* characterization techniques such as transmission electron microscopy (TEM), scanning electron microscopy (SEM), x-ray diffraction (XRD), or temperature programmed desorption (TPD) provide insightful structural information, they are mute on the structure of the surface in the electrochemical environment. Electrochemical scanning tunneling microscopy (ESTM) is a powerful technique for probing flat electrode surfaces *in situ*.[35,36] However, the method is of limited use for the characterization of rough electrodes. Though various x-ray techniques can probe electrode surfaces *in situ*,[22,24,28,37] these methods require synchrotron radiation and can therefore not be employed for routine measurements.

Infrared (IR) spectroscopy has been established as a useful complementary technique for probing the surface structure of heterogeneous catalysts. Specifically, the frequency of the C≡O stretch mode of atop-bound CO (CO_{atop}) is sensitive to the coordination and nature of the metal atom to which CO_{atop} is bound.[38] Therefore, by monitoring the peak frequency of the C≡O stretch band of CO_{atop}, atomic-level structural characteristics of the catalytic surface can be probed.[25,39–44] Because CO_{atop} is an on-pathway intermediate in the electroreduction of CO and CO_2 to hydrocarbons,[45–47] the C≡O stretch frequency could provide atomic-level morphological information on rough metal electrodes under electrocatalytic conditions.

Correlating the C≡O stretch frequency with the structural properties of the electrode during electrolysis is complicated by three factors:

- First, due to experimental constraints, IR and Raman spectroscopies are often carried out under conditions disparate from those employed during electrolysis experiments for the detection of products. For example, in surface-enhanced infrared absorption spectroscopy (SEIRAS), spectra are often taken during a potential sweep on a timescale of a few minutes. By contrast, electrolysis is typically carried out on a timescale of tens of minutes. Electrocatalysts are well-known to undergo surface reconstructions under electrocatalytic conditions.[36,42,48–50] For this reason, spectroscopy often reports on the transient surface characteristics, whereas the measured product distributions are averaged over different states of the electrode surface.

- Second, besides the coordination of the underlying metal atom, the C≡O stretch frequency of CO_{atop} is profoundly affected by the absolute CO coverage on the surface. The coverage affects the frequency in two distinct ways:[38,51] (a) As the coverage changes, the bond energy between CO_{atop} and the surface is altered,[52] thereby modifying the frequency. These effects are termed "chemical effects". (b) The coupling between the dynamical dipoles of CO_{atop} gives rise to new vibrational modes of the coupled system that can greatly affect the observed frequencies and band intensities. These coupling effects increase with increasing coverage. Although information on the surface structure from the C≡O stretch spectra can be obtained despite these coupling effects in certain cases, the extraction of this information can be very challenging and requires elaborate investigations with isotopic mixtures.[53] Therefore, the character of the adsorption site is most straightforwardly revealed by the C≡O stretch frequency of CO_{atop} in the limit of low coverage.[54]

- Third, in the limit of low coverage, where coupling effects are expected to be small, the C≡O stretch frequency of CO_{atop} is generally determined by the character of the adsorption site. For example, in the limit of low coverage of CO_{atop} on copper, the C≡O stretch frequency typically increases with increasing CO_{atop} binding strength to the surface site (Figure S1, Supporting Information (SI)). However, CO_{atop} on copper (111) and (100) surface facets has virtually the same C≡O stretch frequency,[38] even though the binding strength of CO_{atop} is about

40-100 meV larger on the (100) facet.[55,56] Whereas the (111) facet is a poor catalyst for CO and CO_2 reduction, the (100) facet is one of the most active.[57–59] Therefore, it is not straightforward to distinguish between these two surface facets on polycrystalline Cu catalysts on the basis of the C≡O stretch frequency.[55]

Herein, we describe a strategy that overcomes these three challenges. We carried out time-resolved differential electrochemical mass spectrometry (DEMS) and SEIRAS on two types of rough copper electrodes during the reduction of CO. By simultaneously carrying out the two measurements on the same electrode, we were able to connect rigorously the structural information contained in the C≡O stretch spectra with the onset potentials for ethylene formation. Our key findings are as follows:

First, we examined two types of rough, SEIRAS-active electrodes: Electrochemically deposited copper films on Si-supported Au (CuAu-Si) and electrolessly deposited copper on Si (Cu-Si). The CuAu-Si film displays a $\approx 200 \pm 65$ mV more cathodic onset potential for the formation of ethylene in comparison to the Cu-Si film, which suggests that the surface morphologies of the films are distinct. It is often implicitly assumed that SEIRAS-active Cu thin films posses catalytic properties similar to those of polycrystalline Cu foils, which are routinely employed in electrolysis studies. Our finding shows that care has to be taken when comparing results from these Cu thin films with those from Cu foils.

Second, with isotope dilution experiments, we show that the lineshape of the C≡O stretch band at potentials more negative than ≈ -1.0 V versus the Ag/AgCl reference electrode is strongly dominated by the effects of dynamical dipole coupling on both types of SEIRAS-active films. Our finding demonstrates that the saturation coverage of CO_{atop} on the SEIRAS-active electrodes is sufficiently large to give rise to strong dynamical dipole coupling effects. Such effects should be thoroughly considered in the interpretation of future SEIRAS studies, because dynamical dipole coupling obscures surface-structural information contained in the C≡O stretch band.

Third, in contrast to the C≡O stretch band at potentials more negative than ≈ -1.0 V, the evolution of the lineshapes on the two types of films with increasing cathodic potential in the range of -0.6 to ≈ -1.0 V exhibits stark differences. We show that the disparate potential-dependencies of the lineshapes can be explained with a simple Boltzmann model that considers the different binding energies of CO_{atop} on terrace and defect sites. On the basis of this model, we suggest that the different onset potentials for ethylene arise from distinct predominant surface facets on the two films. Specifically, our results indicate that (111) facets predominate on CuAu-Si films, whereas (100) facets are more ubiquitous on Cu-Si films.

Our analysis shows that the observation of the lineshape of the C≡O stretch as a function of applied potential can be utilized to gain insights into the atomic-level structure of rough metal electrodes under electrocatalytic conditions. While we applied this method to two types of SEIRAS-active copper films, it can be broadly applied to other rough metal electrodes. Therefore, the strategy established in this work could be employed to guide the development of preparation methods that yield rough metal electrodes with certain desired preferential surface facets.

Results

Choice and Characteristics of Thin Film Electrodes. Herein, we compare two distinct types of rough and SEIRAS-active thin film electrodes. The first type of copper film was electrolessly deposited on a Si attenuated total internal reflection (ATR) crystal (Cu-Si).[42,46,60] The second type of copper film (≈ 8 nm thick) was electrodeposited onto a gold layer on a Si ATR crystal (CuAu-Si).[61,62] The detailed film preparation protocols are described in the Experimental Procedures section.

We chose to study these films because they represent the most commonly used copper thin films in SEIRAS studies. SEIRAS in

an ATR configuration has become an indispensable technique for probing the electrode/electrolyte interface during CO and CO_2 reduction.[63,64] The physical characteristics of the films enable the facile spectroscopic interrogation of the electrode/electrolyte interface under a wide range of electrochemical conditions. However, because the films tend to peel off from the Si support and undergo surface reconstructions under extended periods of polarization, there is limited information on their catalytic properties.[46,47] For this reason, it is often tacitly assumed that these thin polycrystalline copper films possess catalytic properties similar to those of the polycrystalline copper foils that are routinely employed in electrolysis studies. However, there is no rigorous scientific basis for this assumption. In this work, we characterize the CO reduction activity of these SEIRAS-active copper films.

The nanoscopic surface structures of the two types of films were characterized with atomic force microscopy (AFM) (Figure S2, SI). The AFM images show that Cu-Si films are composed of interconnected particles with an approximate average diameter of 80 nm. The CuAu-Si films show a similar nanoscopic structure, albeit with a smaller average particle size of about 40 nm. The roughness factor (RF) of each film under electrochemical conditions was determined by measuring the capacitance of the electric double layer (Figure S3, SI). The RF is the measured double layer capacitance of the electrode/electrolyte interface compared to that of the interface involving a smooth polycrystalline copper electrode (28 μF cm^{-2}).[65] For Cu-Si and CuAu-Si, typical RFs are ≈ 10 and ≈ 5, respectively. The X-ray diffraction (XRD) spectra of the films show the characteristic peaks of Au, Cu, and Cu_2O (Figure S4, SI).

Onset Potentials for CO Reduction Products for Cu-Si and CuAu-Si. To connect rigorously the electrocatalytic and IR spectroscopic observations for each thin film, we simultaneously conducted DEMS and SEIRAS on the same electrode. The combined DEMS/SEIRAS setup is shown in Scheme 1. Experiments were conducted in aqueous solutions of 0.1 M potassium phosphate at a pH of 7. Before the collection of DEMS/SEIRAS data, the Cu thin films were subjected to three potential cycles between -0.6 and -1.2 V at a scan rate of 0.01 V s^{-1}. This treatment was carried out to remove surface oxides and hydroxides.[47,66] During an experiment, the electrolyte was purged with CO gas at a flow rate of 5 standard cubic centimeter per minute (sccm) and the electrode potential was scanned from -0.6 to -1.8 V at a rate of 0.001 V s^{-1}. Unless otherwise noted, all potentials herein are referenced against the Ag/AgCl electrode. During the scan, IR spectra of the interface and the mass spectra of volatile reduction products evolving from it were concurrently collected with a time resolution of a few seconds. Further experimental details are provided in the Experimental Procedures section.

Figure 1 shows the electrochemical current densities and partial pressures of the ions of hydrogen ($m/z = 2$), methane ($m/z = 15$), and ethylene ($m/z = 26$) for the two types of electrodes. m/z denotes the mass-to-charge ratio of the fragments detected by the mass spectrometer. To account for the differences in the electrochemically active surface areas of the two thin films, all signals in Figure 1 were divided by the RF of the respective electrode.

As shown in Figure 1B, the onset potential for H_2 evolution is ≈ -1.2 V for both types of thin films, indicating that they exhibit comparable water/proton reduction activity. Similarly, the two films have comparable onset potentials for CH_4 evolution (≈ -1.7 V). By contrast, the onset potential for C_2H_4 is $\approx 200 \pm 65$ mV more cathodic for CuAu-Si compared to that for Cu-Si: On Cu-Si and CuAu-Si the onset potentials for C_2H_4 are ≈ -1.4 and ≈ -1.6 V, respectively. Herein, we defined the onset potential of each product as the potential at which the partial pressure of the product is 10% of that at -1.8 V. Choosing a different definition slightly affects the absolute values of the onset potentials, but has no impact on the general tends reported herein. The quoted values are based on four independent experiments for each film. The entire set of experiments is shown in Figure S5 of the SI.

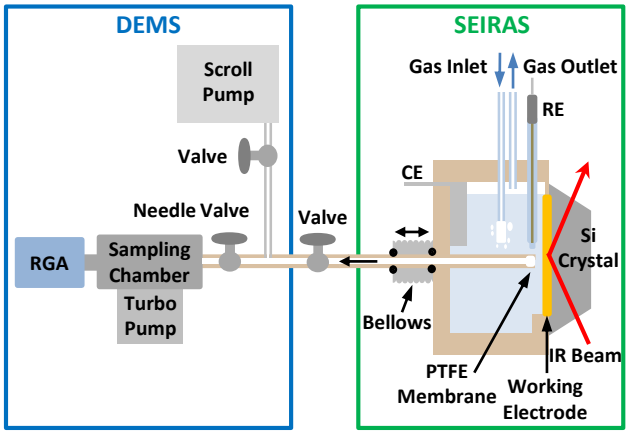

Scheme 1: DEMS/SEIRAS setup. RGA, CE, and RE denote residual gas analyzer, counter electrode, and reference electrode, respectively. The sampling tip was inserted through a polytetrafluoroethylene (PTFE) bellows and connected to a micrometer, enabling the fine adjustment of the tip-electrode distance.

We note that the absolute rates of product formation cannot be accurately determined with this DEMS setup: The partial pressures depend on the tip-electrode distance, which is difficult to precisely reproduce among independent experiments. Like in prior studies where similar setups were employed,[14,67] we therefore restrict the discussion to the onset potentials for the products. Further, our measured onset potentials are somewhat more cathodic than those reported for polycrystalline copper electrodes.[68] While these differences may arise from distinct surface morphologies, the absolute values of the determined onset potentials also depend on the time-resolution of the DEMS setup, which is a complex function of the mass transport of reduction products from the electrode surface to the detector.[69] The exact absolute value of the onset potential is not essential for the following discussion. The key observation herein is that there is a pronounced difference in the onset potentials for ethylene for Cu-Si and CuAu-Si thin film electrodes.

To ensure that the different onset potentials for ethylene are truly due to disparate properties that are intrinsic to the two thin film electrodes, we conducted the following control experiments: (1) The product selectivity for CO reduction is sensitive to the pH of the electrolyte in the vicinity of the electrode.[70–72] Because each electron transfer gives rise to the formation of a hydroxide anion, the interfacial pH may increase during electrocatalysis.[29,73–77] To test if the different onset potentials for ethylene arise from different interfacial pH conditions, we conducted DEMS experiments in aqueous solutions of potassium hydroxide at a pH of 12.85. In this electrolyte, no significant change in the interfacial pH is expected to occur during electrocatalysis. As shown in Figure S6 of the SI, the same trend in ethylene formation is observed. These results suggest that the disparate onset potentials for ethylene for the two types of films do not arise from local pH effects. (2) Exposed gold and/or the formation of a gold/copper alloy may impact the selectivity of the CO reduction reaction.[78,79] To test if the underlying gold substrate is exposed in the CuAu-Si thin film under electrochemical conditions, we employed the C≡O stretch band of CO_{atop} as a probe of the electrochemically active surface. The center frequency of the C≡O stretch band sensitively depends on the chemical identity of the metal substrate and is therefore a suitable probe of exposed gold under electrochemical conditions.[80,81] As shown in Figure S7 of the SI, SEIRAS does not show any evidence for exposed gold. (3) The DEMS signals for ethylene and methane are absent in Ar-purged electrolyte, demonstrating that the signals arise from the reduction of CO (Figure S8, SI).

Taken together, the control experiments suggest that the difference in the onset potentials for ethylene formation on the two thin films arises from intrinsic differences in the copper surfaces. The product selectivity of the reduction of CO to hydrocarbons is sensitive to the surface structure of the electrode.[57–59] Therefore, the more cathodic ethylene onset potential for CuAu-Si compared to that for Cu-Si suggests that the two types of films possess different predominant surface facets.

Analysis of the C≡O Stretch Spectra of CO_{atop} on Cu-Si and CuAu-Si. To gain insights into the surface morphology of the two types of copper thin films, we analyzed the

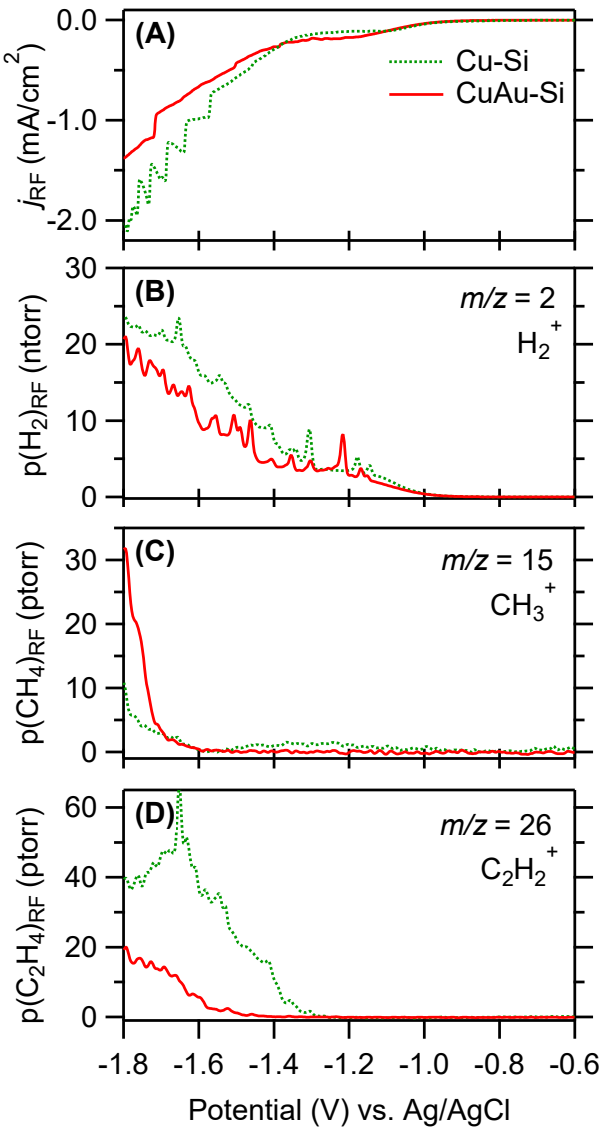

Figure 1: DEMS for Cu-Si and CuAu-Si in contact with CO-saturated 0.1 M potassium phosphate buffer at a pH of 7. (A) Electrochemical current densities. (B) H_2^+ ($m/z = 2$), (C) CH_3^+ ($m/z = 15$), and (D) $C_2H_2^+$ ($m/z = 26$) partial pressures. All signals in this figure were divided by the RF of the respective electrode.

C≡O stretch band of CO_{atop}. The peak frequency of this band is sensitive to the coordination number of the metal atom to which CO_{atop} is bound.[25,39–42,44] The adsorption of CO on late transition metals is partly controlled by the degree of hybridization of the *d*-band of the metal with the π^* orbital of CO.[82–84] The *d*-band shifts to more positive energies with decreasing coordination of the metal sites, resulting in a larger hybridization energy with the π^* orbital. Though a higher degree of hybridization weakens the intramolecular C≡O bond, it does not necessarily result in a lower C≡O stretch frequency: The C≡O stretch frequency of CO_{atop} on Cu blue-shifts with increasing strength of the surface bond (Figure S1, SI). Early theoretical studies suggested that with stronger binding, the surface bond becomes shorter and the carbon atom increasingly oscillates against the surface of the metal.[85,86] This effect, termed the "wall effect", shifts the frequency to higher values. It has been proposed that the relative magnitude of these two opposing effects determines the overall shift.[85]

Apart from the coordination number of the underlying metal atom, the peak frequency of the C≡O stretch band is also affected by "chemical effects" and dynamical dipole coupling.[38,51] As the coverage of CO is modified, the chemical interaction of CO_{atop} with the surface changes. This change in the surface bond affects the frequency. On Cu, this "chemical effect" leads to a decrease in the C≡O stretch frequency with increasing coverage of CO_{atop}.[51] Additionally, the coupling of dynamical dipoles of CO_{atop} gives rise to new normal modes whose band frequencies and intensities are different from those of isolated CO_{atop} molecules in the absence of coupling.[38] "Chemical effects" and dynamical dipole coupling are functions of the surface coverage. We therefore monitored the lineshape as a function of cathodic potential, which changes the coverage of CO_{atop} on the electrode. Further, we conducted experiments with isotopically diluted CO mixtures, where dynamical dipole coupling is partly disrupted.[38]

Figure 2 shows the potential-dependence of the C≡O stretch band of CO_{atop} from −0.87 to −1.05 V. Within this potential range, the most

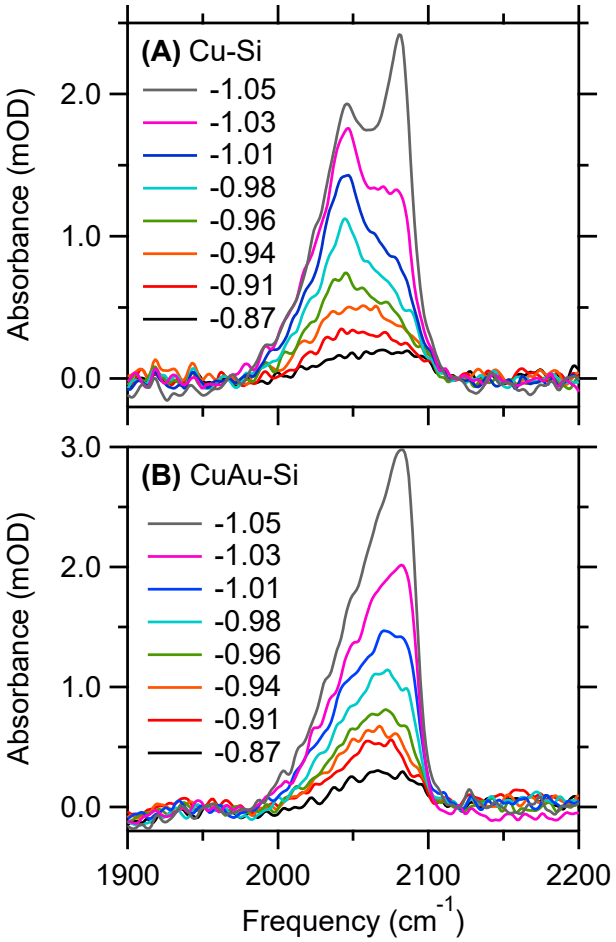

Figure 2: Potential-dependence of the C≡O stretch band of CO_{atop} on (A) Cu-Si and (B) CuAu-Si. The labels in the panels denote the electrode potential in volts versus the Ag/AgCl reference electrode. These spectra were concurrently collected with the DEMS data shown in Figure 1.

significant changes in the lineshape occur. At potentials close to the CO_{atop} saturation coverage (≈ -1.3 V), the changes in lineshape are comparatively small. The evolution of the spectra over the entire potential range is shown in Figure S9 of the SI. The change of the C≡O stretch band with potential is markedly specific to the type of the thin film: For Cu-Si, a prominent band peaked at ≈ 2045 cm^{-1} first develops before a band at ≈ 2080 cm^{-1} steeply gains amplitude with decreasing potential (Figure 2A). By contrast, for CuAu-Si, the band at ≈ 2080 cm^{-1} dominates at all potentials, whereas no distinct band appears at ≈ 2045 cm^{-1} at any potential (Figure 2B). We note that the exact peak positions of the bands depend on the applied potential. In the following, we refer to the band at ≈ 2045 cm^{-1} as the low frequency band (LFB) and the band at ≈ 2080 cm^{-1} as the high frequency band (HFB). Duplicate experiments confirm the reproducibility of the results (Figure S10, SI).

The LFB is attributable to CO_{atop} on terrace sites, whereas the HFB arises from CO_{atop} on defect sites. The peak assignments are well supported by spectroscopic studies on single crystalline copper electrodes: On the Cu(100) electrode in contact with phosphate buffer at neutral pH, the C≡O stretch band of CO_{atop} appears in the range 2040 to 2056 cm^{-1}, depending on the applied potential.[87] For example, the band is centered at a frequency of ≈ 2050 cm^{-1} at a potential of ≈ -1.0 V versus the Ag/AgCl reference electrode. This peak position is in good agreement with the LFB in our spectra (Figure 2A). On polycrystalline Cu, it has been suggested that Cu(100) is the predominant facet under electrochemical conditions.[36,58] It is therefore reasonable to attribute the LFB to CO_{atop} on terrace sites. However, as discussed above, we emphasize that on the basis of the C≡O stretch frequency, it is difficult to distinguish between Cu(100) and Cu(111) terraces. We address the question of the prevalent surface facet further below and in the Discussion section.

On stepped single crystal Cu electrodes in phosphate buffer at neutral pH, the C≡O stretch band of CO_{atop} appears at $\approx 2080 \pm 7$

cm^{-1}, depending on the stepped crystal facet and the applied potential.[88] This band was assigned to CO_{atop} on step sites on the basis of two observations:[88] (a) On Cu(111) single crystal electrodes, the C≡O stretch band of CO_{atop} was not observable. Therefore, for the $n(111)$-(100) single crystal electrodes, the C≡O stretch band could only originate from step sites. (b) The integrated C≡O stretch band area scaled linearly with the step-site density.

Taken together, on the basis of these prior studies of Cu single crystal electrodes under electrolyte and potential conditions similar to those employed in this study, we can confidently assign the LFB and HFB to CO_{atop} on terrace and step (defect) sites, respectively.

The coverage of CO on the electrode is dependent on the mass transport conditions at the electrocatalytic interface. The spectra in Figures 2 were collected in a static electrolyte to enable simultaneous product detection with DEMS (Figure 1). To test if the distinct potential-dependencies of the lineshapes are also observed under different mass transport conditions, we conducted additional experiments in a spectro-electrochemical cell in which the electrolyte was stirred (Figure S11, SI). During these experiments, the potential was scanned from −0.6 to −1.4 V at a rate of 0.002 V s^{-1}. As shown in Figures S12 and S13 of the SI, the same trends were observed. Further, for these experiments, we recorded the spectra for two consecutive cyclic voltammorgams (CV) for each film. No major differences in the lineshapes are noticeable between consecutive cycles. These results demonstrate that the distinct potential-dependencies shown in Figure 2 are observable over a wide range of mass transport conditions and are not due to irreversible processes at the interface (such as irreversible surface reconstructions). These control experiments suggest that at the onset potential for ethylene formation on Cu-Si (≈ −1.4 V), no irreversible surface reconstruction takes place on either of the two thin film electrodes. Although irreversible reconstructions may occur at more cathodic potentials, we can exclude those reconstructions as the origin for the different ethylene onset potentials for the two films on the basis of these experiments. Therefore, the distinct potential-dependencies of the spectra in Figure 2 provide insights into the origin of the different onset potentials for this product on the two types of films.

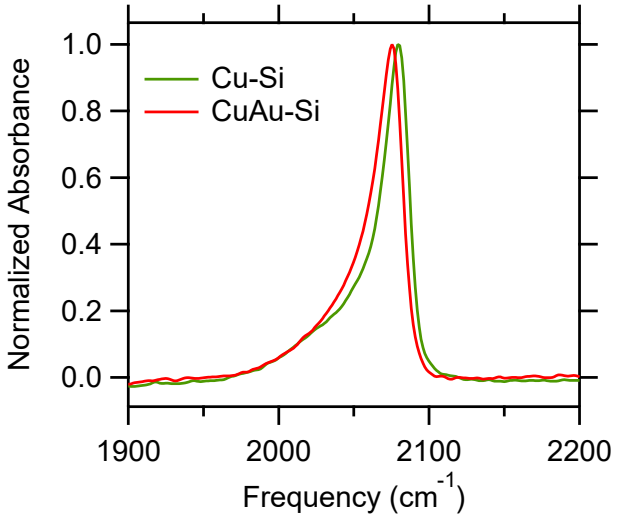

Figure 3: Peak-normalized C≡O stretch band of CO_{atop} on Cu-Si and CuAu-Si at a potential of −1.3 V. The peak amplitudes are 17.2 and 15.2 mOD for the spectra of CO_{atop} on Cu-Si and CuAu-Si, respectively. These spectra were concurrently collected with the DEMS data shown in Figure 1.

Effect of Dynamical Dipole Coupling on the C≡O Stretch Band of CO_{atop}. Figure 3 shows the peak-normalized C≡O stretch bands of CO_{atop} on the two types of films at a potential of −1.3 V, that is, at a potential close to the onset for ethylene formation on Cu-Si. Comparison of the spectra reveals only minute differences: The HFB of CO_{atop} on Cu-Si exhibits a small blue shift of ≈ 5 cm^{-1} with respect to that for CuAu-Si. Further, at ≈ 2045 cm^{-1}, the LFB appears as a shoulder on the HFB in the spectrum of CO_{atop} on Cu-Si. We previously showed that the C≡O stretch band of CO_{atop} can indeed be modeled by the sum of two (skewed) Gaussian functions.[42] Fits of these Gaussian functions to the spectra are shown in Figure S14 of the SI. Given the significant difference in the onset potentials for ethylene formation, the strong similarity between the two spectra may seem surprising. However, as detailed below, dynamical dipole coupling

strongly impacts the spectra in the vicinity of this potential.

The amplitudes of the two Gaussian functions corresponding to the LFB and HFB do not necessarily reflect the relative populations of CO_{atop} on terrace and defect sites: Dynamical dipole coupling can greatly enhance the intensity of the high frequency modes at the expense of the low frequency modes of the coupled system.[38,89] This intensity borrowing amplifies the band that predominantly arises from CO_{atop} on defect sites and attenuates that of CO_{atop} on terrace sites. The strength of dynamical dipole coupling decreases with increasing separation of the singleton frequencies of CO_{atop} (the frequencies in the absence of coupling).[38] Therefore, $^{12}C^{16}O_{atop}$ that is primarily surrounded by $^{13}C^{18}O_{atop}$ will exhibit a lesser degree of dynamical dipole coupling with its neighbors, because the singleton frequencies of the two isotopes are separated by ≈ 100 cm^{-1}.

To assess the degree of dynamical dipole coupling within CO_{atop} adlayers on Cu-Si and CuAu-Si, we conducted SEIRAS of isotopic mixtures of CO. Figure 4A shows the peak-normalized C≡O stretch band of isotopically pure $^{12}C^{16}O_{atop}$ (dashed line) and that of a mixture of 10% $^{12}C^{16}O_{atop}$ and 90% $^{13}C^{18}O_{atop}$ (solid line) on Cu-Si at a potential of −1.3 V. These experiments were carried out in a two-compartment spectro-electrochemical cell under stirring of the electrolyte (Figure S11, SI). The spectrum of the isotopically pure $^{12}C^{16}O_{atop}$ adlayer exhibits the sharp HFB and the broader LFB as a shoulder. As indicated in the figure, the spectrum of the isotopic mixture shows similar bands, labeled HFB_{HI} and LFB_{HI} (the subscript stands for "heavy isotope"). Because these two features primarily arise from $^{13}C^{18}O_{atop}$, they are red-shifted by ≈ 100 cm^{-1} compared to the corresponding bands of the isotopically pure $^{12}C^{16}O_{atop}$ adlayer. Additionally, the spectrum of the isotopic mixture also contains a band centered at ≈ 2045 cm^{-1} (labeled with a star symbol, *), which primarily arises from $^{12}C^{16}O_{atop}$. Clearly, the isotopic mixture does not show a HFB due to the light isotope ($^{12}C^{16}O_{atop}$). This observation indicates that the large amplitude of the HFB in the case of isotopically pure $^{12}C^{16}O_{atop}$ is primarily a result of intensity borrowing due to dynamical dipole coupling. Similar observations can be made for the lineshape of CO_{atop} on CuAu-Si (Figure 4B). Taken together, these results show that dynamical dipole coupling greatly impacts the C≡O stretch band of CO_{atop} on both types of films in a potential range that gives rise to a CO coverage at or close to saturation.

Assessment of Relative CO_{atop} Coverage on Cu-Si and CuAu-Si. We assessed the CO_{atop} coverage on the thin film electrodes. Unfortunately, it is not possible to determine the absolute CO_{atop} coverage on the films: In the case of CO adsorbed on Pt, the absolute coverage of CO is easily determined by electrostripping of the CO adlayer (oxidation of adsorbed CO to CO_2).[90] This method is not applicable here because CO_{atop} on copper is in dynamic equilibrium with solution-phase CO.[42,45,46] Comparison of the integrated C≡O stretch band areas also does not necessarily provide insight into the relative coverages: The surface-enhancement factors may be significantly different between the two types of films. The accurate determination of surface-enhancement factors is a non-trivial task. Further, dynamical dipole coupling leads to deviations from Beer's law.[38,89]

Although the absolute coverage cannot be determined, the relative coverage between the two films can be estimated from the isotope dilution experiments: While dynamical dipole coupling between $^{12}C^{16}O_{atop}$ and $^{13}C^{18}O_{atop}$ is weak, it still occurs because of the broadness of the bands. Dynamical dipole coupling between CO_{atop} molecules of different isotopic composition typically leads to negligible frequency shifts but manifests itself through intensity borrowing.[38] Specifically, the degree of intensity transfer from the bands primarily due to $^{13}C^{18}O_{atop}$ (LFB_{HI} and HFB_{HI} in Figure 4) to the one mostly due to $^{12}C^{16}O_{atop}$ (* in Figure 4) increases with increasing CO_{atop} coverage. Therefore, the ratio of the peak amplitude of HFB_{HI} to that of the (*) band is a semi-quantitative measure of the CO_{atop} coverage. Because this method requires only comparison of relative peak amplitudes within the

same spectrum, variation of the absolute intensity of the spectra from film to film does not affect the following analysis.

Inspection of the spectrum of the isotopic mixture of CO_{atop} on Cu-Si shows that the amplitude of the band primarily associated with $^{12}C^{16}O_{atop}$ (*) is $\approx 30\%$ relative to the amplitude of the HFB_{HI} (Figure 4A; arrows). By contrast, the corresponding band of CO_{atop} on CuAu-Si (*) has only an amplitude of $\approx 10\%$ with respect to the HFB_{HI} peak maximum of the same spectrum (Figure 4B; arrows). This result shows that dynamical dipole coupling is stronger in the case of Cu-Si. We conclude that the saturation coverage of CO_{atop} on Cu-Si is higher in comparison to the coverage on CuAu-Si. Duplicate experiments confirm the reproducibility of the isotope dilution experiments (Figure S15, SI).

Cyclic Voltammetric Characterization of the Surface Facets of Cu-Si and CuAu-Si. The mass spectrometric and spectroscopic data suggest that the two types of films posses distinct predominant crystallographic surface facets. To characterize further the surface facets, we employed cyclic voltammetry (CV). In the CVs of copper single crystals in contact with basic electrolyte, the adsorption and desorption of hydroxide give rise to voltammetric waves whose peak potentials are specific to a certain crystallographic facet.[91–94]

Figures 5A and B respectively show the CVs of Cu(100) and Cu(111) single crystals in contact with Ar-saturated aqueous solutions of 0.1 M KOH. The CVs are not centered around zero on the current density axis because of residual oxygen in the electrolyte.[92] For comparison with prior studies, the potentials in Figure 5 are referenced against the reversible hydrogen electrode (RHE). The peaks in the underpotential region of Cu_2O formation (-0.25 to 0.2 V) are attributable to the adsorption and desorption of hydroxide. The observed peak potentials for the adsorption/desorption of hydroxide are clearly distinct for the two surface facets. Additionally, the magnitude of the oxidation/reduction current density at potentials > 0.3 V is smaller for Cu(111) than for Cu(100). These observations are in good agreement with prior reports.[91–94] Taken together, these features characterize the Cu(111) and Cu(100) surface facets.

Figures 5C and D respectively show the CVs of the Cu-Si and CuAu-Si electrodes. The cathodic scan of the CV for Cu-Si displays a peak at -0.17 V (labeled with a star symbol, *), consistent with the potential of the hydroxide desorption peak for the Cu(100) single crystal. By contrast, the CV for CuAu-Si shows a peak at $+0.07$ V (*) during the anodic scan. This peak falls within the potential range of the hydroxide adsorption peaks for Cu(111). The peaks are not observable on the respective reverse scans, likely because of the sloping baselines and the small amplitudes of these features. At potentials > 0.3 V, the Cu surface is oxidized to Cu_2O. In that region, the shape of the CV for Cu-Si bears a resemblance to that for Cu(100), whereas the shape of the CV for CuAu-Si in that same region is more similar to that for Cu(111).

The CV data suggest that the predominant surface facet on Cu-Si is Cu(100). This conclusion is further supported by prior reports, which showed that the electrocatalytic properties of polycrystalline Cu electrodes are similar to those of Cu(100).[95] Further, electrochemical STEM studies revealed that Cu(100) is a stable facet on polycrystalline Cu under electrocatalytic conditions.[36] By contrast, the CV data indicate that the major facet on CuAu-Si is Cu(111). The predominance of the Cu(111) surface facet on CuAu-Si is likely a result of semi-epitaxial growth of the Cu layer on the Au substrate. As shown in Figure S16 of the SI, the CV of the electrolessly deposited Au film electrode resembles that of a Au(111) electrode.[96] This finding is consistent with prior studies, which found that the electroless deposition of Au on Si results in films that preferentially expose their (111) facet.[96] Epitaxial growth of Cu(111) with a thickness of ≈ 30 nm on Au(111) has been demonstrated for core-shell nanoparticles.[97] Therefore, it is probable that the preferential (111) orientation of the electrochemically deposited Cu layer (≈ 8 nm thick) of the CuAu-Si films arises from its semi-epitaxial growth on the Au(111) sub-

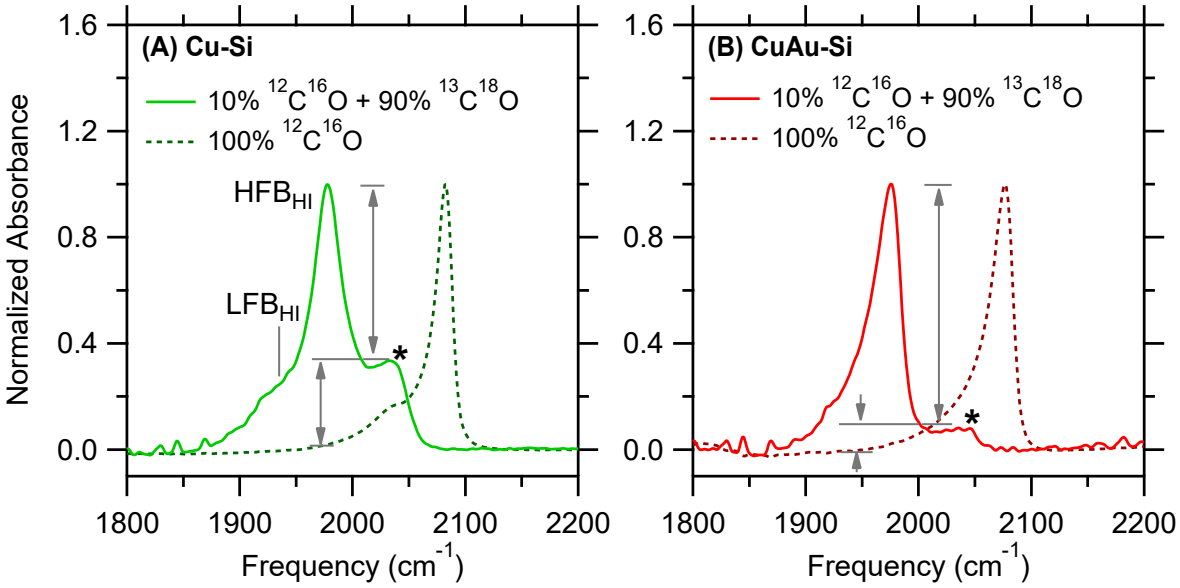

Figure 4: Comparison of the peak-normalized C≡O stretch bands of isotopically pure $^{12}C^{16}O$ and a mixture of 10% $^{12}C^{16}O$ and 90% $^{13}C^{18}O$ adsorbed in the atop configuration on (A) Cu-Si and (B) CuAu-Si at a potential of −1.3 V.

strate. Possible interfacial Cu/Au alloying and surface reconstruction are considered in the Discussion section. In summary, the CV characterization indicates that Cu(100) is the major facet on Cu-Si, whereas Cu(111) is predominant on CuAu-Si.

The *in situ* characterization of the electrode surfaces with the CV method requires alkaline electrolyte. Cu electrodes may undergo reconstruction under alkaline conditions.[36] However, our mass spectrometric control experiments show that the distinct selectivity of Cu-Si and CuAu-Si for ethylene is also observed under alkaline conditions (Figure S6, SI). Further, the distinct potential-dependence of the C≡O stretch spectrum of CO_{atop} is also observed at high pH (Figure S17, SI). On the basis of these control experiments, we conclude that the information on the surface characterization obtained at high pH can be employed for the interpretation of the experiments conducted at neutral pH.

Discussion

The CV characterization suggests that the Cu-Si surface consists mostly of (100) facets, whereas the CuAu-Si surface exhibits mainly (111) facets. On the basis of this result, we can rationalize the potential-dependence of the spectra. The following analysis is based on a simple framework in which we consider only two types of surface sites with different binding affinities for CO_{atop}. Of course, on the polycrystalline electrode, there are many different types of surface sites (edges, kinks, various terraces) that give rise to a distribution of CO_{atop} binding energies. However, this added complexity does not affect the core of our argument. Further, the assumption is justified because the lineshape of the C≡O stretch band at saturation coverage can be modeled by the sum of two Gaussian functions, one representing CO_{atop} on terrace sites, the other CO_{atop} on defect sites (Figure S14, SI).

The relative occupancy of CO_{atop} on defect and terrace sites is governed by the Boltzmann equation:

$$\frac{N_{\text{defect}}}{N_{\text{terrace}}} = \frac{g_{\text{defect}}}{g_{\text{terrace}}} \exp\left(+\frac{\Delta E}{kT}\right), \qquad (1)$$

where g_{defect} and g_{terrace} are the degeneracies of the two types of sites, k is the Boltzmann constant, and T the absolute temperature. $\Delta E = E_{\text{defect}} - E_{\text{terrace}} > 0$ is the difference between

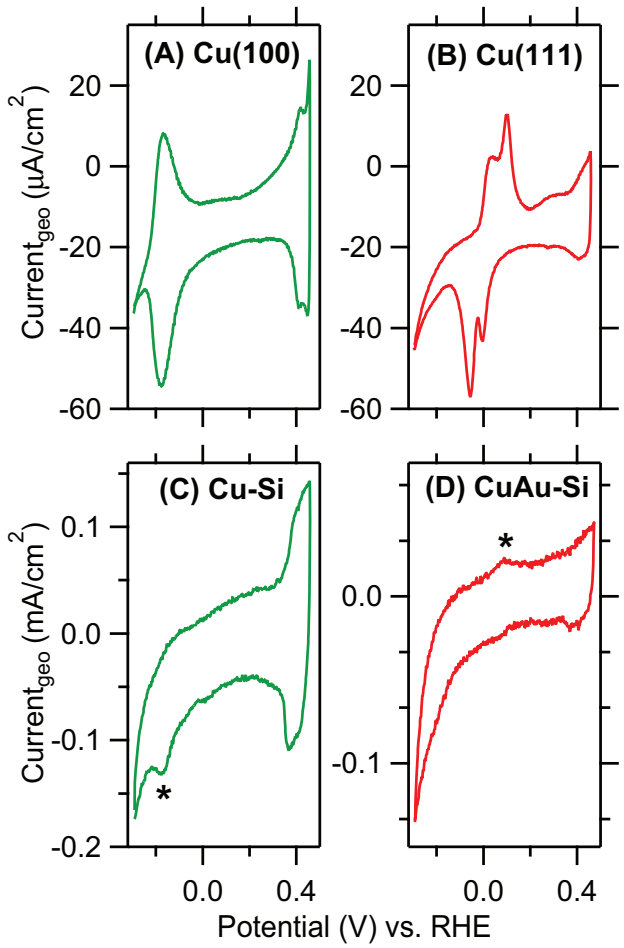

Figure 5: CVs for (A) Cu(100), (B) Cu(111), (C) Cu-Si, and (D) CuAu-Si. The CVs were collected in Ar-saturated 0.1 M KOH at a scan rate of 0.05 V s^{-1}. The panels show the geometric current densities.

the binding energies of CO_{atop} on defect and terrace sites (Herein, we define the binding energies as positive quantities). From eq. (1), it is clear that the relative occupancy is determined by two factors: The relative abundance of defect to terrace sites, $\frac{g_{defect}}{g_{terrace}}$, and the difference in the CO_{atop} binding energy between the two types of sites, ΔE.

We first consider the possibility that the ratio $\frac{g_{defect}}{g_{terrace}}$ could be significantly different for the two types of films. Specifically, the C≡O stretch spectrum of CO_{atop} on CuAu-Si at potentials > -1.0 V may be a result of a higher density of defect sites on that film in comparison to Cu-Si, that is, the ratio $\frac{g_{defect}}{g_{terrace}}$ in eq. (1) may be higher. If CuAu-Si had a substantially higher density of defect sites and an otherwise similar composition of surface facets, a higher CO_{atop} saturation coverage would be observed (relative to that on Cu-Si, because defect sites bind CO_{atop} more strongly). However, the isotope dilution experiments show that the opposite is the case (Figure 4). On the basis of these data, it is unlikely that CuAu-Si possesses a significantly higher defect site density compared to Cu-Si. Therefore, the distinct potential-dependencies of the C≡O stretch spectra on the two types of films likely arise from differences in the exponential term in eq. (1) rather than from different values of $\frac{g_{defect}}{g_{terrace}}$.

By considering the differences in the exponential term in eq. (1), we can understand why the lineshapes of the C≡O stretch exhibit starkly different potential-dependencies for the two types of films. As described in the Results section, the CV characterization indicates that on CuAu-Si, Cu(111) facets predominate, whereas Cu(100) facets prevail on Cu-Si. The experimental energies for the desorption of CO_{atop} from Cu(111) and Cu(100) are 0.49 and 0.53 eV, respectively.[55] DFT calculations predict the same trend for the CO_{atop} binding energies, though the predicted energy difference is about twice as large.[56] On both films, we assume that the binding energy of CO_{atop} on defect sites is 0.60 eV, the experimentally determined desorption energy of CO_{atop} from polycrystalline copper surfaces as determined by temperature programmed desorption.[55] This

assumption is justified because this value is similar to that observed for CO_{atop} desorption from step edges on Cu(211).[55]

On the basis of these values, ΔE in eq. (1) is smaller for Cu-Si than for CuAu-Si. As a result, according to eq. (1), the probability for CO to occupy a terrace site is about five times higher on Cu-Si than that on CuAu-Si at room temperature. This population of CO_{atop} on (100) terrace sites manifests itself in the IR spectrum as the C≡O stretch band at 2045 cm^{-1}, which dominates the spectrum at potentials > -1.0 V (Figure 2A). Once a certain threshold coverage has been reached, dynamical dipole coupling amplifies the band associated with CO_{atop} on defect sites, producing the marked change in lineshape around -1.0 V. By contrast, on CuAu-Si, the large difference in binding energies between (111) terrace and defect sites prevents the buildup of a significant population of CO_{atop} on terrace sites. As a result, even at relatively anodic potentials, the band exhibits a higher peak frequency due to the binding of CO to defect sites (Figure 2B). Figure 6 summarizes this analysis.

The model provides a simple explanation for the disparate evolution of the C≡O stretch spectrum on the two film types. Importantly, the analysis establishes the potential-dependence of the C≡O stretch band of CO_{atop} as a suitable probe of the atomic-level surface morphology of rough electrodes. As discussed above, the peak frequency of the C≡O stretch band is often a complex function of coupling effects and the applied potential. Because our analysis presented here focuses on general trends of the lineshape rather than exact numerical values, we expect this method to be more robust and versatile than an analysis that solely focuses on peak frequencies.

Taken as a whole, the CV characterization and the spectroscopic data indicate that (100) terraces are prevalent on Cu-Si, whereas (111) terraces are more ubiquitous on CuAu-Si. This finding is consistent with our DEMS results that show that the onset potential for ethylene is $\approx 200 \pm 65$ mV more cathodic for CuAu-Si compared to that for Cu-Si: In prior studies, DEMS on single crystalline copper electrodes in phosphate buffer at a pH of 7 showed that the onset potential for ethylene formation on Cu(111) is about 200 mV more cathodic than that on Cu(100).[58,59,70] This trend does not only hold for Cu(111) and Cu(100), but it is more general. Single crystals on which the (111) facet predominates exhibit more cathodic onset potentials for ethylene formation than crystals on which the (100) facet is more abundant.[59] Similarly, the F.E. for ethylene during the reduction of CO_2 in 0.1 M $KHCO_3$ on Cu(111) electrodes is about five times lower than that on Cu(100).[57]

Consideration of Alternative Explanations. The relatively high C≡O stretch frequency on CuAu-Si at potentials > -1.0 V could also arise from the formation of CO islands, that is, a non-uniform distribution of CO on the surface. Such island formation would enable dynamical dipole coupling even at low absolute coverage. Islands of CO were observed on single crystalline Pt electrodes when the coverage was lowered from saturation by partial oxidation of the CO adlayer.[90] Spatially non-uniform oxidation of the CO adlayer then results in patches of CO on the electrode. In the case of CO_{atop} on Cu-Si, island formation is unlikely: DFT calculations and experiment work showed that the interaction between neighboring CO molecules is highly repulsive.[52,98] Unlike in the case of Pt, CO_{atop} is reversibly bound to copper and in dynamic equilibrium with solution-phase CO.[42,45,46] Therefore, CO_{atop} island formation on Cu is less likely than on Pt electrodes.

To confirm this notion, we monitored the potential-dependence of the C≡O stretch band of the light isotope in a mixture of 50% $^{12}C^{16}O_{atop}$ and 50% $^{13}C^{18}O_{atop}$. In this mixture, we can observe the band of the light isotope at potentials > -1.0 V. As shown in Figure S18 of the SI, at a potential of -0.93 V, isotopic dilution has essentially no effect on the peak frequency of the band arising from $^{12}C^{16}O_{atop}$. This experiment confirms that the comparatively high frequency of this band at potentials > -1.0 V is mostly due to adsorption of CO on defect sites. Dynamical dipole coupling does not make a major contribution at these rela-

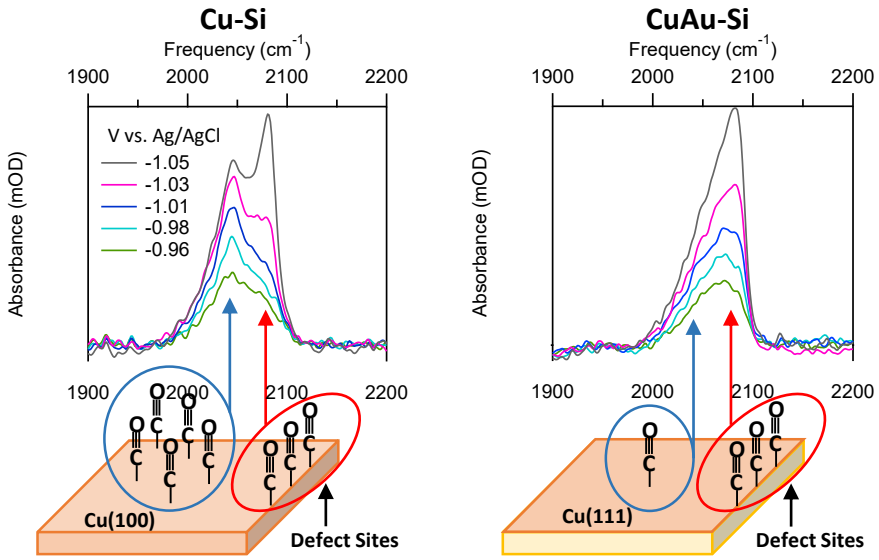

Figure 6: Cartoon summarizing the key findings. Cu-Si (Left): Because the difference in CO_{atop} binding energy between (100) terrace and defect sites is relatively small, a significant CO_{atop} population develops on the terraces. This CO population gives rise to the band at 2045 cm^{-1}. CuAu-Si (Right): The difference in CO_{atop} adsorption energy between (111) terrace and defect sites is comparatively large for CuAu-Si. As a result, the CO_{atop} population on terraces remains small, preventing the development of a distinct band at 2045 cm^{-1}.

tively anodic potentials.

We note that in a recent study on the mass transport effects of CO on the spectrum of CO_{atop}, Malkani *et al.* concluded that CO adsorbs on Cu in islands.[99] The spectra of Malkani *et al.* exhibit different lineshapes in comparison to ours. This observation indicates that their film morphology is different from those of our films. Further, they conducted their work at a more cathodic potential (−0.6 V versus RHE). It is entirely possible that CO island formation occurs on their electrodes and experimental conditions, whereas it does not in our experiments. Therefore, our findings do not contradict their conclusions. The possibility that the formation of CO_{atop} islands on Cu could be potential-dependent is intriguing and warrants further investigation.

The isotope dilution experiments presented here show that dynamical dipole coupling strongly influences the lineshape at potentials more cathodic than ≈ −1.0 V. However, it is not the sole contributing factor. In an earlier publication,[42] we presented evidence that a CO-induced, reversible surface reconstruction process also contributes to the change in lineshape with decreasing potential. For example, the concurrent enhancement of the metal-adsorbate bands and the HFB in the surface-enhanced Raman spectra reported in that work cannot be explained with a dynamical dipole coupling picture, but is consistent with an adsorbate-induced reconstruction process. While such a reconstruction process adds complexity to the picture, it does not impact the qualitative aspects of the model presented herein.

Recently, it was suggested that co-adsorbed hydroxide on Cu electrodes lowers the C≡O stretch frequency and influences the binding energy of adsorbed CO.[66,100] Specifically, Iijima *et al.* showed that the lineshape of the C≡O stretch mode of CO_{atop} on Cu electrodes is profoundly dependent on the number of CVs (−0.13 and −0.7 V) that are performed as a pre-treatment prior to spectroscopic measurements.[66] With an increasing number of CVs (from zero to 15), they observed an increase in the C≡O stretch frequency. They attributed this observation to a decrease in the coverage of hydroxide with increasing number of CV pre-treatments.

In our experiments, we pre-treated each electrode with five cleaning CVs between −0.13 and −0.7 V, followed by three CVs with turning potentials of −0.6 and −1.2 V prior to the collection of SEIRAS/DEMS data (see Experimental Procedures Section for details). Following these steps, we ensured that the electrode was never returned to oxidizing potentials until the end of the experiment. The following observations suggest that this protocol is effective in minimizing the impact of hydroxide on the C≡O stretch spectrum: First, to test if the spectra are sensitive to the number of CV pre-treatments, we collected additional SEIRAS data in which we increased the number of cleaning CVs (−0.13 and −0.7 V) from 5 to 15. All other steps of the protocol were left unchanged. Iijima *et al.* suggested that this treatment minimizes the amount of hydroxide on the surface.[66] As shown in Figure S19 of the SI, the potential-dependencies of the spectra shown in Figure 2 (5 CV pre-treatments) are also observed after 15 CV pre-treatments. Second, to probe if the spectra change with an increase in the bulk hydroxide concentration, we carried out SEIRAS on the two films in contact with 0.1 M phosphate buffer at a pH of 12. As shown in Figure S17 of the SI, we observed similar potential-dependencies of the spectra as reported in Figure 2. This finding shows that an increase of the bulk hydroxide concentration by five orders of magnitude does not significantly impact the lineshape. Third, the changes in lineshape with potential are reversible on both types of films and are also observed during consecutive CV cycles (Figures S12 and S13, SI). Fourth, from the hydroxide desorption waves in the CVs in Figure 5, the hydroxide desorption potentials for Cu(100) and Cu(111) are −0.78 and −0.67 V vs. Ag/AgCl at neutral pH, respectively. Because we examined the potential-dependence of the spectra at more negative potentials, the amount of hydroxide on the surface is expected to be minimal.

Taken together, these observations suggest that the impact of hydroxide on the lineshape of the C≡O stretch band of CO_{atop} on Cu is minimal under our experimental conditions. However, it is possible that co-adsorbed hydroxide is a small contributing factor. Indeed, a possible contribution of hydroxide would be consistent with our conclusion that on Cu-Si, the major surface facet is (100). As shown in Figure 5, the desorption potential of hydroxide is ≈ 0.1 V more cathodic for Cu(100) compared to that for Cu(111). Therefore, the appearance of the LFB band on Cu-Si may be in part because of co-adsorbed hydroxide, but this effect is expected to be small on the bases of the observations discussed in the preceding paragraph.

Different coverages of bridge-bonded CO (CO_{bridge}, referring to adsorbed CO interacting with two or three Cu surface atoms) on Cu-Si and CuAu-Si could influence the onset potential of ethylene. Recent studies showed that CO_{bridge} on Cu electrodes is an electrochemically inactive species under CORR/CO_2RR conditions.[47,101] For the data presented herein, the amplitude of the band of CO_{bridge} was close to the detection limit on both types of films during the cathodic forward scans under neutral pH conditions, suggesting that CO_{bridge} does not give rise to the different catalytic activities of the films.

Lastly, we consider the possibility that the Cu overlayer may be affected by strain and ligand effects.[102–104] Our CV characterization of CuAu-Si suggests that the surface is of Cu(111) character (Figure 5). Indeed, pseudomorphic Cu overlayers on Au(111) substrates have been imaged with electrochemical STM.[105] However, overlayers of Cu on Au have a tendency to coalesce into islands and to form interfacial Cu/Au alloys under cathodic polarization.[43,105,106] Although our SEIRAS control experiments did not reveal the presence of Au on the surface (Figure S7, SI), the amount of Au at the surface may be below the detection limit of the method. Because Cu/Au alloys bind CO less strongly than pure Cu,[43,107] the incorporation of Au into Cu terraces of the CuAu-Si films is an alternative explanation for the absence of a distinct LFB on that electrode.

Semi-epitaxial growth of Cu on Au(111) and any strain or ligand effects are expected to be limited to thin overlayers. Indeed, for CuAu-Si electrode with a 16 nm thick Cu overlayer, the potential-dependence of the C≡O stretch band

resembles that observed for Cu-Si (Figure S20, SI), suggesting the CuAu-Si system as a convenient SEIRAS platform to study the impact of Cu overlayer thickness on catalyst selectivity.

Conclusions

We showed that the two most commonly used methods for the deposition of SEIRAS-active copper films on Si result in electrode surfaces that exhibit greatly different catalytic activities towards the reduction of CO to ethylene: Films produced by the electrochemical deposition of copper on Si-supported Au thin films (CuAu-Si) display a $\approx 200 \pm 65$ mV more cathodic onset potential for the formation of ethylene compared to that of Cu thin films that are electrolessly deposited on the Si support (Cu-Si).

Despite the great difference in CO reduction activity, in the vicinity of the potential of CO_{atop} saturation coverage (-1.3 V), the C≡O stretch bands of CO_{atop} on CuAu-Si and Cu-Si are remarkably similar. SEIRAS of isotopically diluted mixture of CO_{atop} show that the C≡O stretch lineshape at the saturation coverage is profoundly influenced by dynamical dipole coupling on both films. However, the degree of dynamical dipole coupling on CuAu-Si is lower than in the case of Cu-Si, suggesting a higher CO_{atop} surface coverage on the latter film. Further, the potential-dependence of the lineshape of the C≡O stretch band at potentials > -1.0 V is remarkably different for the two thin films. We rationalize the potential-dependence of the spectra with a Boltzmann model that considers the difference in CO adsorption energy on defect sites and the sites of the prevalent crystallographic surface facet. On the basis of this model, we conclude that the major surface facet on Cu-Si binds CO more strongly than that on CuAu-Si. Based on our CV characterization of the electrodes and our electrocatalytic results, we suggest that the prevalent crystallographic facet on CuAu-Si is (111), whereas that on Cu-Si is (100). Our study highlights the complexities involved in the interpretation of the C≡O stretch band of CO_{atop} on polycrystalline copper electrodes. Further, our work shows that the analysis of the potential-dependence of the C≡O stretch lineshape can reveal differences in the surface structure of electrocatalysts under electrocatalytic conditions. This strategy could be employed to guide the design of rough electrodes with certain desired surface facets.

Experimental Procedures

Materials. Chemicals for Cu or Au thin film deposition on Si: NH_4F (40 wt.% in H_2O), HF (48 wt.%), $NaAuCl_4 \cdot 2H_2O$ (99.99%; metals basis), Na_2SO_3 (98.5%; for analysis, anhydrous), $Na_2S_2O_3 \cdot 2H_2O$ (99.999%; trace metal basis), and NH_4Cl (99.999%; metal basis) were purchased from Fisher Scientific (Waltham, MA). $CuSO_4 \cdot 5H_2O$ (99.999%; trace metal basis), EDTA-Na_2 ($99.0-101.0$%; ACS Reagent), 2,2-bipyridine ($\geq$ 99%; ReagentPlus), HCHO (35 wt.%; 10% methanol as stabilizer), and NaOH (99.99%; trace metals basis) were acquired from Sigma Aldrich (St. Louis, MO). Polycrystalline diamond pastes and alumina slurry were procured from Ted Pella (Redding, CA) or Electron Microscopy Sciences (Hartfield, PA).

Chemicals for electrochemical measurements: (KH_2PO_3, $\geq$ 99.995%, TraceSELECT, metals basis; K_2HPO_3, $\geq$ 99.999%, TraceSELECT, metals basis; KOH, 99.99%, trace metals basis, Sigma Aldrich). High-purity water for electrolyte preparation was derived from a Barnstead Nanopure Diamond system.

Ar (ultra high purity), N_2 (ultra high purity), and CO (99.999%) were obtained from Air Gas (Radnor, PA). Doubly labeled $^{13}C^{18}O$ (99 atom % ^{13}C, 95 atom % ^{18}O) was purchased from Sigma Aldrich.

Cu(100) and Cu(111) single crystals ($5 \times 5 \times 1$ mm) were purchased from MTI Corporation (Richmond, CA).

Cu-Si Film Deposition. Thin polycrystalline Cu-Si films were deposited in an electroless manner on the reflecting surface of a 60° Si prism (Pike Technologies; Madison, WI) as previously described.[108] The thin Cu films had a resistance of $3-5$ Ω.

CuAu-Si Film Deposition. Thin polycrystalline Au films were first deposited in an electroless manner on the reflecting surface of a 60° Si prism (Pike Technologies; Madison, WI) according to established procedures.[61,62] The Si crystal was cleaned with aqua regia solution to remove Au residue prior to each deposition. To prepare the Si crystal surface, it was successively polished with 6 and 1 μm diamond pastes and 1 μm alumina slurry on a polishing pad. Then, the crystal was rinsed under high-purity water and sonicated in water or acetone alternately for 5 times. For deposition, the Si crystal was first etched in 40 % NH_4F for 90 s to remove surface oxides and to terminate the surface with hydrogen. A gold nanofilm was plated by immersing the Si crystal in a 2 : 1 mixture of a plating solution and 2% HF at 60°C for 120 s. The plating solution contained 15 mM $NaAuCl_4{\cdot}2H_2O$, 150 mM Na_2SO_3, 50 mM $Na_2S_2O_3{\cdot}2H_2O$, and 50 mM NH_4Cl. To improve Au film adhesion to the Si crystal, the deposited Au film was removed by placing a few drops of aqua regia on the film.[96] Then, the Si crystal was thoroughly washed with high-purity water and dried with ultra high-purity nitrogen. On this Si crystal, a second gold nanofilm was plated by immersing the crystal in the plating solution as described above. Removal and re-deposition of the Au film was repeated until a homogeneous film was obtained. Typically, the second or third re-deposition yielded a stable gold nanofilm on the Si crystal. The deposited Au thin films had a resistance of $8 - 10\ \Omega$.

The Au film was cleaned with five CVs in 0.1 M H_2SO_4 solution from 0 to 1.5 V at a scan rate of 0.05 V s^{-1} under 5 sccm Ar purging. Then, the Cu electrodeposition was carried out with an addition of 5.75 mM $CuSO_4$ to the solution. The film was held at a potential of −0.2 V until the desired amount of charge (≈ 40 mC) was passed. The thickness of the film was calculated according to: $t_{\mathrm{Cu}} = \frac{Q_{\mathrm{Cu}} \cdot m_{\mathrm{Cu}}}{zFA\rho}$, where Q_{Cu}, $\mathrm{m_{Cu}}$, z, F, A, and ρ represent the total charge during deposition, Cu atomic mass, electrons needed per Cu atom deposition, Faraday constant, deposition area, and Cu film density, respectively. The CuAu-Si film was then rinsed with high-purity water.

Pre-treatment of Cu-Si and CuAu-Si Films Prior to DEMS and SEIRAS Experiments. Prior to the collection of DEMS and SEIRAS data, Cu-Si and CuAu-Si were pre-treated according to the following protocol: With the cell at open circuit, the electrolyte was purged with Ar for 20 minutes at a rate of 5 sccm. The electrode was then treated with five CVs from −0.13 to −0.7 V vs. Ag/AgCl at a scan rate of 0.05 V s^{-1} followed by the RF determination. To determine the RF of the film, the capacitance of the electrochemical double layer in Ar saturated electrolyte (Figure S3, SI) was measured as previously described.[108] Immediately after this step, Cu film was subjected to three CVs from −0.6 to −1.2 V at a 0.01 V s^{-1} scan rate. Following this step, the Cu electrode was never returned to oxidizing potentials until the end of the DEMS/SEIRAS experiments. After completion of the CVs, potential was held at −0.6 V in the 0.1 M phosphate buffer electrolytes and at −0.8 V in 0.1 M KOH for 20 min while CO was purged at a rate of 5 sccm.

DEMS/SEIRAS Measurements. The components of the DEMS setup were described previously.[108] The DEMS setup in this work only differed in the configuration and positioning mechanism of the sampling tip within the spectro-electrochemical cell (Scheme 1). The sampling tip was positioned ≈ 100 μm above the electrode surface. A single compartment spectro-electrochemical cell was used as shown in Figure 1. The catholyte volume was 6 mL. Prior to each experiment, the cell was cleaned for 1 h in an acid solution (30 wt.% H_2SO_4, 30 wt.% HNO_3) and afterwards sonicated for 1 h in Nanopure water. A Ag/AgCl (RE-5B, 3 M NaCl; BASi Inc.; West Lafayette, IN) and a Pt foil (Premion 99.99%, 0.025 mm; Alfa Aesar) were utilized as the reference and counter electrodes, respectively. The Ag/AgCl reference electrode was regularly checked against a saturated calomel electrode (CHI 150; CH Instruments Inc.; Austin, TX). The spectroscopic methods were described previously.[108] Following the pre-treatment steps described above, the DEMS/SEIRAS experiments were conducted. For the combined DEMS/SEIRAS experiments in 0.1 M phosphate buffer, the po-

tential was scanned from −0.6 to −1.8 V at a rate of 0.001 V s^{-1}. In 0.1 M KOH, the potential was scanned from −0.8 to −1.8 V at the same rate.

Isotope Dilution Measurements. Isotope dilution experiments were carried out with gas mixtures of either 90% $^{13}C^{18}O$ + 10% $^{12}C^{16}O$ or 50% $^{13}C^{18}O$ + 50% $^{12}C^{16}O$. The electrolyte was purged with 4.5 sccm of $^{13}C^{18}O$ and 0.5 sccm of $^{12}C^{16}O$ to produce a 90% : 10% mixture. To obtain the 50% : 50% mixture both $^{13}C^{18}O$ and $^{12}C^{16}O$ were purged at a rate of 2.5 sccm. Then, the potential was scanned from −0.6 to −1.4 V at a rate of 0.002 V s^{-1} in CO-saturated electrolyte while SEIRAS spectra were collected. These experiments were carried out in the spectro-electrochemical cell shown in Figure S11 of the SI under stirring of the electrolyte.

Cyclic Voltammetric Characterization of Cu Surfaces. The backsides of the Cu(100) and Cu(111) single crystals were covered with epoxy. Prior to CV characterization, the single crystal electrodes were cleaned electrochemically in an acid solution of H_3PO_4:H_2SO_4:H_2O = 10 : 5 : 2. A potential of 2.3 V vs. Cu was applied for 2 s followed by 30 s at open circuit potential and another 2 s at 2.3 V. The electrodes were then thoroughly rinsed with high-purity water before they were immersed in an Ar saturated 0.1 M KOH solution. CVs of Cu(100) and Cu(111) were collected in a single compartment cell while the electrolyte was purged with Ar gas at a rate of 5 sccm. The electrolyte was stirred. Ten CV cycles were collected from −0.3 to 0.45 V vs. RHE at a 0.05 V s^{-1} scan rate and the 10^{th} cycle is shown in Figure 5. CVs of the Cu-Si and CuAu-Si films were collected in Ar saturated 0.1 M KOH in the cell shown in Figure S11 of SI under stirring of the electrolyte. The Cu-Si and CuAu-Si films were pre-treated by applying five CVs with turning potentials of −0.13 and −0.7 V at a scan rate of 0.05 V s^{-1}. This step was followed by capacitance measurements to determined the RF of each film (Figure S3, SI). Then, 10 CVs were collected from −0.3 to 0.45 V versus RHE at a 0.05 V s^{-1} scan rate while Ar was purged at a rate of 5 sccm. The 10^{th} cycle is shown in Figure 5. Similar CV shapes as those shown in Figure 5 were also observed in the other cycles.

Supporting Information Available

Literature data showing the dependence of the C≡O stretch frequency on the CO_{atop} desorption energy. Characterization of the films with AFM, double layer capacitance measurements, and X-ray diffraction. Repeat DEMS measurements in CO-saturated phosphate buffer at pH 7. DEMS in CO-saturated 0.1 M KOH. Spectra of CuAu-Si film from −0.3 to −1.4 V in CO-saturated phosphate buffer at pH 7. DEMS for Cu-Si in Ar-saturated phosphate buffer at pH 7. Spectra concurrently collected with DEMS in Figure 1. Additional SEIRAS spectra concurrently collected during DEMS experiments. Scheme of two-compartment SEIRAS cell. SEIRAS of Cu-Si and CuAu-Si for consecutive CVs. Lineshape analysis of the C≡O stretch band. Duplicates of the experiments in Figure 4 with isotopic mixtures. CV of the Au-Si film. SEIRAS spectra in phosphate buffer at pH 12. Spectra in a mixture of 50% $^{12}C^{16}O$ and 50% $^{13}C^{18}O$ and isotopically pure $^{12}C^{16}O$ on CuAu-Si. SEIRAS spectra after 15 CV pretreatments. SIERAS of a 16 nm CuAu-Si film in 0.1 M phosphate buffer at pH 7.

This information is available free of charge on the ACS Publication website.

Acknowledgement This work was supported by a CAREER award from the National Science Foundation (Award No.: CHE-1847841). J.L. was partly supported by the US Department of Energy's Basic Energy Sciences - Solar Photochemistry Program (Award No.: DE-SC0020261). We thank Professor Eric Borguet for suggesting the experiments with doubly labeled carbon monoxide.

References

(1) Manthiram, K.; Beberwyck, B. J.; Alivisatos, A. P. Enhanced Electrochemical Methanation of Carbon Dioxide with

a Dispersible Nanoscale Copper Catalyst. *J. Am. Chem. Soc.* **2014**, *136*, 13319–13325.

(2) Kim, C.; Jeon, H. S.; Eom, T.; Jee, M. S.; Kim, H.; Friend, C. M.; Min, B. K.; Hwang, Y. J. Achieving Selective and Efficient Electrocatalytic Activity for CO_2 Reduction Using Immobilized Silver Nanoparticles. *J. Am. Chem. Soc.* **2015**, *137*, 13844–13850.

(3) Loiudice, A.; Lobaccaro, P.; Kamali, E. A.; Thao, T.; Huang, B. H.; Ager, J. W.; Buonsanti, R. Tailoring Copper Nanocrystals Towards C_2 Products in Electrochemical CO_2 Reduction. *Angew. Chem. Int. Ed.* **2016**, *55*, 5789–5792.

(4) Kim, D.; Kley, C. S.; Li, Y.; Yang, P. Copper Nanoparticle Ensembles for Selective Electroreduction of CO_2 to C2–C3 Products. *Proc. Natl. Acad. Sci. U.S.A.* **2017**, *114*, 10560–10565.

(5) Kauffman, D. R.; Alfonso, D. R.; Tafen, D. N.; Wang, C.; Zhou, Y.; Yu, Y.; Lekse, J. W.; Deng, X.; Espinoza, V.; Trindell, J.; Ranasingha, O. K.; Roy, A.; Lee, J.-S.; Xin, H. L. Selective Electrocatalytic Reduction of CO_2 into CO at Small, Thiol-Capped Au/Cu Nanoparticles. *J. Phys. Chem. C* **2018**, *122*, 27991–28000.

(6) Li, C. W.; Kanan, M. W. CO_2 Reduction at Low Overpotential on Cu Electrodes Resulting from the Reduction of Thick Cu_2O Films. *J. Am. Chem. Soc.* **2012**, *134*, 7231–7234.

(7) Kas, R.; Kortlever, R.; Yilmaz, H.; Koper, M. T. M.; Mul, G. Manipulating the Hydrocarbon Selectivity of Copper Nanoparticles in CO_2 Electroreduction by Process Conditions. *ChemElectroChem* **2015**, *2*, 354–358.

(8) Ma, M.; Trześniewski, B. J.; Xie, J.; Smith, W. A. Selective and Efficient Reduction of Carbon Dioxide to Carbon Monoxide on Oxide-Derived Nanostructured Silver Electrocatalysts. *Angew. Chem. Inter. Ed.* **2016**, *55*, 9748–9752.

(9) Dutta, A.; Rahaman, M.; Luedi, N. C.; Mohos, M.; Broekmann, P. Morphology Matters: Tuning the Product Distribution of CO_2 Electroreduction on Oxide-Derived Cu Foam Catalysts. *ACS Catal.* **2016**, *6*, 3804–3814.

(10) Raciti, D.; Cao, L.; Livi, K. J. T.; Rottmann, P. F.; Tang, X.; Li, C.; Hicks, Z.; Bowen, K. H.; Hemker, K. J.; Mueller, T.; Wang, C. Low-Overpotential Electroreduction of Carbon Monoxide Using Copper Nanowires. *ACS Catal.* **2017**, *7*, 4467–4472.

(11) Lv, J.-J.; Jouny, M.; Luc, W.; Zhu, W.; Zhu, J.-J.; Jiao, F. A Highly Porous Copper Electrocatalyst for Carbon Dioxide Reduction. *Adv. Mater.* **2018**, *30*, 1803111.

(12) Wang, L.; Nitopi, S.; Wong, A. B.; Snider, J. L.; Nielander, A. C.; Morales-Guio, C. G.; Orazov, M.; Higgins, D. C.; Hahn, C.; Jaramillo, T. F. Electrochemically Converting Carbon Monoxide to Liquid Fuels by Directing Selectivity with Electrode Surface Area. *Nat. Catal.* **2019**, *2*, 702–708.

(13) Chen, C. S.; Handoko, A. D.; Wan, J. H.; Ma, L.; Ren, D.; Yeo, B. S. Stable and Selective Electrochemical Reduction of Carbon Dioxide to Ethylene on Copper Mesocrystals. *Catal. Sci. Technol.* **2015**, *5*, 161–168.

(14) Roberts, F. S.; Kuhl, K. P.; Nilsson, A. High Selectivity for Ethylene from Carbon Dioxide Reduction over Copper Nanocube Electrocatalysts. *Angew. Chem. Int. Ed.* **2015**, *54*, 5179–5182.

(15) Kwon, Y.; Lum, Y.; Clark, E. L.; Ager, J. W.; Bell, A. T. CO_2 Electroreduction with Enhanced Ethylene and Ethanol Selectivity by Nanostructuring Polycrystalline Copper. *ChemElectroChem* **2016**, *3*, 1012–1019.

(16) Gao, D.; Scholten, F.; Cuenya, B. R. Improved CO_2 Electroreduction Performance on Plasma-Activated Cu Catalysts via Electrolyte Design: Halide Effect. *ACS Catal.* **2017**, *7*, 5112–5120.

(17) Reller, C.; Krause, R.; Volkova, E.; Schmid, B.; Neubauer, S.; Rucki, A.; Schuster, M.; Schmid, G. Selective Electroreduction of CO_2 Toward Ethylene on Nano Dendritic Copper Catalysts at High Current Density. *Adv. Energy Mater.* **2017**, *7*, 1602114.

(18) Gao, D.; Sinev, I.; Scholten, F.; Arán-Ais, R. M.; Divins, N. J.; Kvashnina, K.; Timoshenko, J.; Roldan Cuenya, B. Selective CO_2 Electroreduction to Ethylene and Multicarbon Alcohols via Electrolyte-Driven Nanostructuring. *Angew. Chem. Inter. Ed.* **2019**, *58*, 17047–17053.

(19) Hoang, T. T. H.; Ma, S.; Gold, J. I.; Kenis, P. J. A.; Gewirth, A. A. Nanoporous Copper Films by Additive-Controlled Electrodeposition: CO_2 Reduction Catalysis. *ACS Catal.* **2017**, *7*, 3313–3321.

(20) Liu, M. et al. Enhanced Electrocatalytic CO_2 Reduction via Field-Induced Reagent Concentration. *Nature* **2016**, *537*, 382–386.

(21) Chen, X.; Henckel, D.; Nwabara, U.; Li, Y.; Frenkel, A. I.; Fister, T. T.; Kenis, P. J. A.; Gewirth, A. A. Controlling Speciation during CO_2 Reduction on Cu-Alloy Electrodes. *ACS Catal.* **2020**, *10*, 672–682.

(22) De Luna, P.; Quintero-Bermudez, R.; Dinh, C.-T.; Ross, M. B.; Bushuyev, O. S.; Todorovic, P.; Regier, T.; Kelley, S. O.; Yang, P.; Sargent, E. H. Catalyst Electro-Redeposition Controls Morphology and Oxidation State for Selective Carbon Dioxide Reduction. *Nat. Catal.* **2018**, *1*, 103–110.

(23) Yoon, Y.; Hall, A. S.; Surendranath, Y. Tuning of Silver Catalyst Mesostructure Promotes Selective Carbon Dioxide Conversion into Fuels. *Angew. Chem. Int. Ed.* **2016**, *55*, 15282–15286.

(24) Nguyen-Phan, T.-D.; Wang, C.; Marin, C. M.; Zhou, Y.; Stavitski, E.; Popczun, E. J.; Yu, Y.; Xu, W.; Howard, B. H.; Stuckman, M. Y.; Waluyo, I.; Ohodnicki, P. R.; Kauffman, D. R. Understanding Three-dimensionally Interconnected Porous Oxide-Derived Copper Electrocatalyst for Selective Carbon Dioxide Reduction. *J. Mater. Chem. A* **2019**, *7*, 27576–27584.

(25) Malkani, A. S.; Dunwell, M.; Xu, B. Operando Spectroscopic Investigations of Copper and Oxide-Derived Copper Catalysts for Electrochemical CO Reduction. *ACS Catal.* **2019**, *9*, 474–478.

(26) Reske, R.; Mistry, H.; Behafarid, F.; Cuenya, B. R.; Strasser, P. Particle Size Effects in the Catalytic Electroreduction of CO_2 on Cu Nanoparticles. *J. Am. Chem. Soc.* **2014**, *136*, 6978–6986.

(27) Mistry, H.; Varela, A. S.; Kühl, S.; Strasser, P.; Cuenya, B. R. Nanostructured Electrocatalysts with Tunable Activity and Selectivity. *Nat. Rev. Mater.* **2016**, *1*, 16009.

(28) Eilert, A.; Cavalca, F.; Roberts, F. S.; Osterwalder, J.; Liu, C.; Favaro, M.; Crumlin, E. J.; Ogasawara, H.; Friebel, D.; Pettersson, L. G. M.; Nilsson, A. Subsurface Oxygen in Oxide-Derived Copper Electrocatalysts for

Carbon Dioxide Reduction. *J. Phys. Chem. Lett.* **2017**, *8*, 285–290.

(29) Raciti, D.; Mao, M.; Park, J. H.; Wang, C. Local pH Effect in the CO_2 Reduction Reaction on High-Surface-Area Copper Electrocatalysts. *J. Electrochem. Soc.* **2018**, *165*, F799–F804.

(30) Verdaguer-Casadevall, A.; Li, C. W.; Johansson, T. P.; Scott, S. B.; McKeown, J. T.; Kumar, M.; Stephens, I. E. L.; Kanan, M. W.; Chorkendorff, I. Probing the Active Surface Sites for CO Reduction on Oxide-Derived Copper Electrocatalysts. *J. Am. Chem. Soc.* **2015**, *137*, 9808–9811.

(31) Mistry, H.; Varela, A. S.; Bonifacio, C. S.; Zegkinoglou, I.; Sinev, I.; Choi, Y.-W.; Kisslinger, K.; Stach, E. A.; Yang, J. C.; Strasser, P.; Cuenya, B. R. Highly Selective Plasma-Activated Copper Catalysts for Carbon Dioxide Reduction to Ethylene. *Nat. Commun.* **2016**, *7*, 12123.

(32) Ren, D.; Deng, Y.; Handoko, A. D.; Chen, C. S.; Malkhandi, S.; Yeo, B. S. Selective Electrochemical Reduction of Carbon Dioxide to Ethylene and Ethanol on Copper(I) Oxide Catalysts. *ACS Catal.* **2015**, *5*, 2814–2821.

(33) Lum, Y.; Ager, J. W. Stability of Residual Oxides in Oxide-Derived Copper Catalysts for Electrochemical CO_2 Reduction Investigated with ^{18}O Labeling. *Angew. Chem. Int. Ed.* **2018**, *57*, 551–554.

(34) Mandal, L.; Yang, K. R.; Motapothula, M. R.; Ren, D.; Lobaccaro, P.; Patra, A.; Sherburne, M.; Batista, V. S.; Yeo, B. S.; Ager, J. W.; Martin, J.; Venkatesan, T. Investigating the Role of Copper Oxide in Electrochemical CO_2 Reduction in Real Time. *ACS Appl. Mater. Interfaces* **2018**, *10*, 8574–8584.

(35) Gewirth, A. A.; Niece, B. K. Electrochemical Applications of in Situ Scanning Probe Microscopy. *Chem. Rev.* **1997**, *97*, 1129–1162.

(36) Kim, Y.-G.; Baricuatro, J. H.; Javier, A.; Gregoire, J. M.; Soriaga, M. P. The Evolution of the Polycrystalline Copper Surface, First to Cu(111) and Then to Cu(100), at a Fixed CO_2RR Potential: A Study by Operando EC-STM. *Langmuir* **2014**, *30*, 15053–15056.

(37) Firet, N. J.; Blommaert, M. A.; Burdyny, T.; Venugopal, A.; Bohra, D.; Longo, A.; Smith, W. A. Operando EXAFS Study Reveals Presence of Oxygen in Oxide-Derived Silver Catalysts for Electrochemical CO_2 Reduction. *J. Mater. Chem. A* **2019**, *7*, 2597–2607.

(38) Hollins, P.; Pritchard, J. Infrared Studies of Chemisorbed Layers on Single Crystals. *Prog. Surf. Sci.* **1985**, *19*, 275–349.

(39) Zou, S.; Gomez, R.; Weaver, M. J. Infrared Spectroscopy of Carbon Monoxide at the Ordered Palladium (110)-Aqueous Interface: Evidence for Adsorbate-Induced Surface Reconstruction. *Surf. Sci.* **1998**, *399*, 270–283.

(40) Pischel, J.; Pucci, A. Low-Temperature Adsorption of Carbon Monoxide on Gold Surfaces: IR Spectroscopy Uncovers Different Adsorption States on Pristine and Rough Au(111). *J. Phys. Chem. C* **2015**, *119*, 18340–18351.

(41) Eren, B.; Liu, Z.; Stacchiola, D.; Somorjai, G. A.; Salmeron, M. Structural Changes of Cu(110) and Cu(110)-(2 $\times$ 1)-O Surfaces under Carbon Monoxide in the Torr Pressure Range Studied with Scanning Tunneling Microscopy and Infrared Reflection Absorption Spectroscopy. *J. Phys. Chem. C* **2016**, *120*, 8227–8231.

(42) Gunathunge, C. M.; Li, X.; Li, J.; Hicks, R. P.; Ovalle, V. J.; Waegele, M. M. Spectroscopic Observation of Reversible Surface Reconstruction

of Copper Electrodes Under CO_2 Reduction. *J. Phys. Chem. C* **2017**, *121*, 12337–12344.

(43) Ross, M. B.; Dinh, C. T.; Li, Y.; Kim, D.; De Luna, P.; Sargent, E. H.; Yang, P. Tunable Cu Enrichment Enables Designer Syngas Electrosynthesis from CO_2. *J. Am. Chem. Soc.* **2017**, *139*, 9359–9363.

(44) Patel, D. A.; Hannagan, R. T.; Kress, P. L.; Schilling, A. C.; Cinar, V.; Sykes, E. C. H. Atomic-Scale Surface Structure and CO Tolerance of NiCu Single-Atom Alloys. *J. Phys. Chem. C* **2019**, *123*, 28142–28147.

(45) Hori, Y.; Murata, A.; Yoshinami, Y. Adsorption of CO, Intermediately Formed in Electrochemical Reduction of CO_2, at a Copper Electrode. *J. Chem. Soc., Faraday Trans.* **1991**, *87*, 125–128.

(46) Wuttig, A.; Liu, C.; Peng, Q.; Yaguchi, M.; Hendon, C. H.; Motobayashi, K.; Ye, S.; Osawa, M.; Surendranath, Y. Tracking a Common Surface-Bound Intermediate During CO_2-to-Fuels Catalysis. *ACS Cent. Sci.* **2016**, *2*, 522–528.

(47) Gunathunge, C. M.; Ovalle, V. J.; Li, Y.; Janik, M. J.; Waegele, M. M. Existence of an Electrochemically Inert CO Population on Cu Electrodes in Alkaline pH. *ACS Catal.* **2018**, *8*, 7507–7516.

(48) Matsushima, H.; Taranovskyy, A.; Haak, C.; Gründer, Y.; Magnussen, O. M. Reconstruction of Cu(100) Electrode Surfaces during Hydrogen Evolution. *J. Am. Chem. Soc.* **2009**, *131*, 10362–10363.

(49) Yan, B.; Krishnamurthy, D.; Hendon, C. H.; Deshpande, S.; Surendranath, Y.; Viswanathan, V. Surface Restructuring of Nickel Sulfide Generates Optimally Coordinated Active Sites for Oxygen Reduction Catalysis. *Joule* **2017**, *1*, 600–612.

(50) Medina-Ramos, J.; Zhang, W.; Yoon, K.; Bai, P.; Chemburkar, A.; Tang, W.; Atifi, A.; Lee, S. S.; Fister, T. T.; Ingram, B. J.; Rosenthal, J.; Neurock, M.; van Duin, A. C. T.; Fenter, P. Cathodic Corrosion at the Bismuth–Ionic Liquid Electrolyte Interface under Conditions for CO_2 Reduction. *Chem. Mater.* **2018**, *30*, 2362–2373.

(51) Woodruff, D.; Hayden, B.; Prince, K.; Bradshaw, A. Dipole Coupling and Chemical Shifts in IRAS of CO Adsorbed on Cu(110). *Surf. Sci.* **1982**, *123*, 397–412.

(52) Mason, S. E.; Grinberg, I.; Rappe, A. M. Adsorbate-Adsorbate Interactions and Chemisorption at Different Coverages Studied by Accurate ab initio Calculations: CO on Transition Metal Surfaces. *J. Phys. Chem. B* **2006**, *110*, 3816–3822.

(53) Browne, V.; Fox, S.; Hollins, P. Infrared Spectroscopy as an In Situ Probe of Morphology. *Catal. Today* **1991**, *9*, 1–14.

(54) Sheppard, N.; Nguyen, T. T. Chapter 2: Vibrational Spectra of Carbon Monoxide Chemisorbed on the Surfaces of Metal Catalysts - A Suggested Scheme of Interpretation. In *Advances in Infrared and Raman Spectroscopy: v. 5*; Clark, R. J. H., Hester, R. E., Eds.; Heyden, 1978; pp 67–148.

(55) Vollmer, S.; Witte, G.; Wöll, C. Determination of Site Specific Adsorption Energies of CO on Copper. *Catal. Lett.* **2001**, *77*, 97–101.

(56) Mason, S. E.; Grinberg, I.; Rappe, A. M. First-Principles Extrapolation Method for Accurate CO Adsorption Energies on Metal Surfaces. *Phys. Rev. B* **2004**, *69*, 161401.

(57) Hori, Y.; Takahashi, I.; Koga, O.; Hoshi, N. Electrochemical Reduction of Carbon Dioxide at Various Series of Copper Single Crystal Electrodes. *J. Mol. Catal. A: Chem.* **2003**, *199*, 39–47.

(58) Schouten, K.; Qin, Z.; Pérez Gallent, E.; Koper, M. T. M. Two Pathways for the Formation of Ethylene in CO Reduction on Single-Crystal Copper Electrodes. *J. Am. Chem. Soc.* **2012**, *134*, 9864–9867.

(59) Schouten, K.; Pérez Gallent, E.; Koper, M. Structure Sensitivity of the Electrochemical Reduction of Carbon Monoxide on Copper Single Crystals. *ACS Catal.* **2013**, *3*, 1292–1295.

(60) Wang, H.-F.; Yan, Y.-G.; Huo, S.-J.; Cai, W.-B.; Xu, Q.-J.; Osawa, M. Seeded Growth Fabrication of Cu-on-Si Electrodes for In Situ ATR-SEIRAS Applications. *Electrochim. Acta* **2007**, *52*, 5950–5957.

(61) Miyake, H.; Ye, S.; Osawa, M. Electroless Deposition of Gold Thin Films on Silicon for Surface-Enhanced Infrared Spectroelectrochemistry. *Electrochem. Commun.* **2002**, *4*, 973–977.

(62) Heyes, J.; Dunwell, M.; Xu, B. CO_2 Reduction on Cu at Low Overpotentials with Surface-Enhanced in Situ Spectroscopy. *J. Phys. Chem. C* **2016**, *120*, 17334–17341.

(63) Zhu, S.; Li, T.; Cai, W.-B.; Shao, M. CO_2 Electrochemical Reduction As Probed through Infrared Spectroscopy. *ACS Energy Lett.* **2019**, *4*, 682–689.

(64) Kas, R.; Ayemoba, O.; Firet, N. J.; Middelkoop, J.; Smith, W. A.; Cuesta, A. In-Situ Infrared Spectroscopy Applied to the Study of the Electrocatalytic Reduction of CO_2: Theory, Practice and Challenges. *ChemPhysChem* **2019**, *20*, 2904–2925.

(65) Waszczuk, P.; Zelenay, P.; Sobkowski, J. Surface Interaction of Benzoic Acid with a Copper Electrode. *Electrochim. Acta* **1995**, *40*, 1717–1721.

(66) Iijima, G.; Inomata, T.; Yamaguchi, H.; Ito, M.; Masuda, H. Role of a Hydroxide Layer on Cu Electrodes in Electrochemical CO_2 Reduction. *ACS Catal.* **2019**, *9*, 6305–6319.

(67) Pérez-Gallent, E.; Marcandalli, G.; Figueiredo, M. C.; Calle-Vallejo, F.; Koper, M. T. M. Structure- and Potential-Dependent Cation Effects on CO Reduction at Copper Single-Crystal Electrodes. *J. Am. Chem. Soc.* **2017**, *139*, 16412–16419.

(68) Schouten, K.; Kwon, Y.; van der Ham, C.; Qin, Z.; Koper, M. A New Mechanism for the Selectivity to C_1 and C_2 Species in the Electrochemical Reduction of Carbon Dioxide on Copper Electrodes. *Chem. Sci.* **2011**, *2*, 1902–1909.

(69) Jambunathan, K.; Hillier, A. C. Measuring Electrocatalytic Activity on a Local Scale with Scanning Differential Electrochemical Mass Spectrometry. *J. Electrochem. Soc.* **2003**, *150*, E312–E320.

(70) Schouten, K. J. P.; Pérez Gallent, E.; Koper, M. T. M. The Influence of pH on the Reduction of CO and CO_2 to Hydrocarbons on Copper Electrodes. *J. Electroanal. Chem.* **2014**, *716*, 53–57.

(71) Roberts, F. S.; Kuhl, K. P.; Nilsson, A. Electroreduction of Carbon Monoxide over a Copper Nanocube Catalyst: Surface Structure and pH Dependence on Selectivity. *ChemCatChem* **2016**, *8*, 1119–1124.

(72) Wang, L.; Nitopi, S. A.; Bertheussen, E.; Orazov, M.; Morales-Guio, C. G.; Liu, X.; Higgins, D. C.; Chan, K.; Nørskov, J. K.; Hahn, C., et al. Electrochemical Carbon Monoxide Reduction on Polycrystalline Copper: Effects of Potential, Pressure, and pH on Selectivity Toward Multicarbon and Oxygenated Products. *ACS Catal.* **2018**, *8*, 7445–7454.

(73) Singh, M. R.; Clark, E. L.; Bell, A. T. Effects of Electrolyte, Catalyst, and

Membrane Composition and Operating Conditions on the Performance of Solar-Driven Electrochemical Reduction of Carbon Dioxide. *Phys. Chem. Chem. Phys.* **2015**, *17*, 18924–18936.

(74) Ayemoba, O.; Cuesta, A. Spectroscopic Evidence of Size-Dependent Buffering of Interfacial pH by Cation Hydrolysis during CO_2 Electroreduction. *ACS Appl. Mater. Inter.* **2017**, *9*, 27377–27382.

(75) Dunwell, M.; Yang, X.; Setzler, B. P.; Anibal, J.; Yan, Y.; Xu, B. Examination of Near-Electrode Concentration Gradients and Kinetic Impacts on the Electrochemical Reduction of CO_2 using Surface-Enhanced Infrared Spectroscopy. *ACS Catal.* **2018**, *8*, 3999–4008.

(76) Zhang, F.; Co, A. C. Direct Evidence of Local pH Change and the Role of Alkali Cation during CO_2 Electroreduction in Aqueous Media. *Angew. Chem. Inter. Ed.* **2019**, *58*, 2–10.

(77) Yang, K.; Kas, R.; Smith, W. A. In Situ Infrared Spectroscopy Reveals Persistent Alkalinity near Electrode Surfaces during CO_2 Electroreduction. *J. Am. Chem. Soc.* **2019**, *141*, 15891–15900.

(78) Mistry, H.; Reske, R.; Strasser, P.; Cuenya, B. R. Size-Dependent Reactivity of Gold-Copper Bimetallic Nanoparticles During CO_2 Electroreduction. *Catal. Today* **2017**, *288*, 30–36.

(79) Kim, C.; Dionigi, F.; Beermann, V.; Wang, X.; Möller, T.; Strasser, P. Alloy Nanocatalysts for the Electrochemical Oxygen Reduction (ORR) and the Direct Electrochemical Carbon Dioxide Reduction Reaction (CO_2RR). *Adv. Mater.* **2019**, *31*, 1805617.

(80) Wuttig, A.; Yaguchi, M.; Motobayashi, K.; Osawa, M.; Surendranath, Y. Inhibited Proton Transfer Enhances Au-Catalyzed CO_2-to-Fuels Selectivity. *Proc. Natl. Acad. Sci. U. S. A.* **2016**, *113*, E4585–E4593.

(81) Dunwell, M.; Lu, Q.; Heyes, J. M.; Rosen, J.; Chen, J. G.; Yan, Y.; Jiao, F.; Xu, B. The Central Role of Bicarbonate in the Electrochemical Reduction of Carbon Dioxide on Gold. *J. Am. Chem. Soc.* **2017**, *139*, 3774–3783.

(82) Hammer, B.; Morikawa, Y.; Nørskov, J. K. CO Chemisorption at Metal Surfaces and Overlayers. *Phys. Rev. Lett.* **1996**, *76*, 2141–2144.

(83) Chorkendorff, I.; Niemantsverdriet, J. W. *Concepts of Modern Catalysis and Kinetics*; John Wiley & Sons, Weinheim, Germany, 2017.

(84) Mason, S. E.; Grinberg, I.; Rappe, A. M. Orbital-Specific Analysis of CO Chemisorption on Transition-Metal Surfaces. *J. Phys. Chem. C* **2008**, *112*, 1963–1966.

(85) Bagus, P.; Pacchioni, G. Electric Field Effects on the Surface-Adsorbate Interaction: Cluster Model Studies. *Electrochim. Acta* **1991**, *36*, 1669–1675.

(86) Head-Gordon, M.; Tully, J. C. Electric Field Effects on Chemisorption and Vibrational Relaxation of CO on Cu(100). *Chem. Phys.* **1993**, *175*, 37–51.

(87) Hori, Y.; Koga, O.; Watanabe, Y.; Matsuo, T. FTIR Measurements of Charge Displacement Adsorption of CO on Poly- and Single Crystal (100) of Cu Electrodes. *Electrochim. Acta* **1998**, *44*, 1389–1395.

(88) Koga, O.; Teruya, S.; Matsuda, K.; Minami, M.; Hoshi, N.; Hori, Y. Infrared Spectroscopic and Voltammetric Study of Adsorbed CO on Stepped Surfaces of Copper Monocrystalline Electrodes. *Electrochim. Acta* **2005**, *50*, 2475–2485.

(89) Borguet, E.; Dai, H. Site-specific Properties and Dynamical Dipole Coupling of CO Molecules Adsorbed on a Vicinal Cu(100) Surface. *J. Chem. Phys.* **1994**, *101*, 9080–9095.

(90) Chang, S.-C.; Weaver, M. J. Coverage-Dependent Dipole Coupling for Carbon Monoxide Adsorbed at Ordered Platinum(111)-Aqueous Interfaces: Structural and Electrochemical Implications. *J. Chem. Phys.* **1990**, *92*, 4582–4594.

(91) Jović, V.; Jović, B. EIS and Differential Capacitance Measurements onto Single Crystal Faces in Different Solutions: Part II: Cu(111) and Cu(100) in 0.1 M NaOH. *J. Electroanal. Chem.* **2003**, *541*, 13–21.

(92) Schouten, K. J. P.; Gallent, E. P.; Koper, M. T. The Electrochemical Characterization of Copper Single-Crystal Electrodes in Alkaline Media. *J. Electroana. Chem.* **2013**, *699*, 6–9.

(93) Le Duff, C. S.; Lawrence, M. J.; Rodriguez, P. Role of the Adsorbed Oxygen Species in the Selective Electrochemical Reduction of CO_2 to Alcohols and Carbonyls on Copper Electrodes. *Angew. Chem. Int. Ed.* **2017**, *56*, 12919–12924.

(94) Bagger, A.; Arán-Ais, R. M.; Halldin Stenlid, J.; Campos dos Santos, E.; Arnarson, L.; Degn Jensen, K.; Escudero-Escribano, M.; Cuenya, B. R.; Rossmeisl, J. Ab Initio Cyclic Voltammetry on Cu (111), Cu (100) and Cu (110) in Acidic, Neutral and Alkaline Solutions. *ChemPhysChem* **2019**, *20*, 3096–3105.

(95) Hori, Y.; Wakebe, H.; Tsukamoto, T.; Koga, O. Adsorption of CO Accompanied with Simultaneous Charge Transfer on Copper Single Crystal Electrodes Related with Electrochemical Reduction of CO_2 to Hydrocarbons. *Surf. Sci.* **1995**, *335*, 258–263.

(96) Yaguchi, M.; Uchida, T.; Motobayashi, K.; Osawa, M. Speciation of Adsorbed Phosphate at Gold Electrodes: A Combined Surface-Enhanced Infrared Absorption Spectroscopy and DFT Study. *J. Phys. Chem. Lett.* **2016**, *7*, 3097–3102.

(97) Tsuji, M.; Yamaguchi, D.; Matsunaga, M.; Alam, M. J. Epitaxial Growth of Au@Cu Core- Shell Nanocrystals Prepared Using the PVP-Assisted Polyol Reduction Method. *Cryst. Growth Des.* **2010**, *10*, 5129–5135.

(98) Ellis, J.; Toennies, J. P.; Witte, G. Helium Atom Scattering Study of the Frustrated Translation Mode of CO Adsorbed on the Cu(001) Surface. *J. Chem. Phys.* **1995**, *102*, 5059–5070.

(99) Malkani, A. S.; Li, J.; Anibal, J.; Lu, Q.; Xu, B. Impact of Forced Convection on Spectroscopic Observations of the Electrochemical CO Reduction Reaction. *ACS Catal.* **2020**, *10*, 941–946.

(100) Dinh, C.-T.; Burdyny, T.; Kibria, M. G.; Seifitokaldani, A.; Gabardo, C. M.; García de Arquer, F. P.; Kiani, A.; Edwards, J. P.; De Luna, P.; Bushuyev, O. S.; Zou, C.; Quintero-Bermudez, R.; Pang, Y.; Sinton, D.; Sargent, E. H. CO_2 Electroreduction to Ethylene via Hydroxide-Mediated Copper Catalysis at an Abrupt Interface. *Science* **2018**, *360*, 783–787.

(101) Chou, T.-C.; Chang, C.-C.; Yu, H.-L.; Yu, W.-Y.; Dong, C.-L.; Velasco-Vélez, J.-J.; Chuang, C.-H.; Chen, L.-C.; Lee, J.-F.; Chen, J.-M.; Wu, H.-L. Controlling the Oxidation State of the Cu Electrode and Reaction Intermediates for Electrochemical CO_2 Reduction to Ethylene. *J. Am. Chem. Soc.* **2020**, *142*, 2857–2867.

(102) Reske, R.; Duca, M.; Oezaslan, M.; Schouten, K. J. P.; Koper, M. T. M.; Strasser, P. Controlling Catalytic Selectivities during CO_2 Electroreduction on Thin Cu Metal Overlayers. *J. Phys. Chem. Lett.* **2013**, *4*, 2410–2413.

(103) Varela, A. S.; Schlaup, C.; Jovanov, Z. P.; Malacrida, P.; Horch, S.; Stephens, I.

E. L.; Chorkendorff, I. CO_2 Electroreduction on Well-Defined Bimetallic Surfaces: Cu Overlayers on Pt(111) and Pt(211). *J. Phys. Chem. C* **2013**, *117*, 20500–20508.

(104) Clark, E. L.; Hahn, C.; Jaramillo, T. F.; Bell, A. T. Electrochemical CO_2 Reduction over Compressively Strained CuAg Surface Alloys with Enhanced Multi-Carbon Oxygenate Selectivity. *J. Am. Chem. Soc.* **2017**, *139*, 15848–15857.

(105) Schlaup, C.; Horch, S.; Chorkendorff, I. On the Stability of Copper Overlayers on Au(111) and Au(100) Electrodes under Low Potential Conditions and in the Presence on CO and CO_2. *Surf. Sci.* **2015**, *631*, 155–164.

(106) Friebel, D.; Mbuga, F.; Rajasekaran, S.; Miller, D. J.; Ogasawara, H.; Alonso-Mori, R.; Sokaras, D.; Nordlund, D.; Weng, T.-C.; Nilsson, A. Structure, Redox Chemistry, and Interfacial Alloy Formation in Monolayer and Multilayer Cu/Au(111) Model Catalysts for CO_2 Electroreduction. *J. Phys. Chem. C* **2014**, *118*, 7954–7961.

(107) Wang, W.; Shi, H.; Wang, L.; Li, Z.; Shi, H.; Wu, K.; Shao, X. Comparison Study of Structural Properties and CO Adsorption on the Cu/Au(111) and Au/Cu(111) Thin Films. *J. Phys. Chem. C* **2018**, *122*, 19551–19559.

(108) Li, J.; Li, X.; Gunathunge, C. M.; Waegele, M. M. Hydrogen Bonding Steers the Product Selectivity of Electrocatalytic CO Reduction. *Proc. Natl. Acad. Sci. USA* **2019**, *116*, 9220–9229.

Graphical TOC Entry